University of Oklahoma

Graduate College

Geometric Phase, Zeeman, and Optical Effects in the Excitation of PbF and Kr

A Dissertation

Submitted to the Graduate Faculty

in partial fullfillment of the requirements for the

degree of

Doctor of Philosophy

By

PRIYANKA MILINDA RUPASINGHE
Norman, Oklahoma
2011

Geometric Phase, Zeeman, and Optical Effects in the Excitation of PbF and Kr

A Dissertation Approved for the
Homer L. Dodge Department of Physics and Astronomy

By

Dr. Neil E. Shafer-Ray, Chair

Dr. Eric R. I. Abraham

Dr. Gregory Parker

Dr. Patrick Skubic

Dr. Wai Tak Yip

© Copyright PRIYANKA MILINDA RUPASINGHE, 2011
All Rights Reserved.

කුඩා කල සිට මා ළඟින් සිට

දහසක් කැපකිරීම් මැද

මා දිරිමත් කළ

මගේ ආදරණීය දෙමාපියන්ට

සෙනෙහසින් පිළිගැන්වෙයි ...

This dissertation is dedicated to my loving parents,

who always encouraged me to pursue higher education and

dedicated their lives for our future...

Acknowledgements

I owe my deepest gratitude to my thesis advisor Prof. Neil Shafer-Ray for his guidance, encouragement and support given throughout my PhD. This thesis would not have been possible unless his supervision. I was lucky enough to work with such a brilliant mind. Thanks for accepting me to your research group many years ago and being a fabulous advisor. Your patience and dedication to me was the key thing behind this success, where I am today.

My sincere gratitude to rest of the committee Prof. Eric Abraham, Prof. Gregory Parker, Prof. Patrick Skubic and Prof. Wai Tak Yip (Department of Chemistry and Bio-Chemistry) to willingness to being a committee member and providing numerous support, guidance and encouragement during this long journey. Specially, I would like to thank Prof. Eric Abraham allowing me to use his laboratory for optical excitation of Kr experiment and support and guidance given in the initial setup process.

My sincere thanks to our collaborators Prof. Jens Uwe Grabow and Prof. Richard Mawhorter for spending their valuable time in order to take Zeeman data of PbF. As a result precise and complete characterization of ground state of PbF has been published. I am grateful to Prof. Jens Uwe Grabow for providing me some figures describing the apparatus used in the experiment in Hanover, Germany.

I would like to thank my laboratory partners Dr. Sivakumar Poopalasingham and Dr. Christopher McRaven for their help and support given to me when I was a beginner to the Shafer-ray lab few years ago. We worked as a team, thanks for the nice friendship that made me more comfortable in the lab. I would also like to thank

graduate students and laboratory partners Tao Yang, James Coker, Haoquan Fan for their support and friendship. I feel the continuation of our envision experiment to measure the electron electric dipole moment left in good hands. Many thanks to Prof. John Moore-Furnaux for helping and guiding us specially building the new vacuum system in the lab. My sincere thanks also goes to graduate student Dahal Parshuram for his support given to the Kr experiment while I was working in Prof. Abraham's laboratory specially in the initial setup process.

I would like to acknowledge the professional staff of the department for their support in numerous ways. Joel Young, Barry Bergeron, Sean Attebury in the machine shop for designing and building of valuable experimental apparatus and parts which were essential to do our experiments. Adrienne Wade in the electronic shop for providing me a much better environment for building electronics. Your knowledge, support and experience were always benefited me. Danette Loyd, Debbie Barnhill and Sharon Widner in the front office for working hard for keeping the department running smoothly. You may not notice, however, it is essential to do research.

I would like to show my gratitude to all of my teachers from the childhood and specially my high school physics teacher Mr. A. Abeydheera and my undergraduate advisor Dr. S. R. D. Rosa for making me physics interest. Thank you all for guiding and helping me towards this long journey to a PhD.

I owe my deepest gratitude to my brother, sister and parents for their patience and dedication. Specially, I am grateful to my loving parents for their encouragement and support given to me even in some hard times of my family. Without you all this success

is unthinkable. I am indebted to my loving wife Priyangi for her encouragement and dedication during all ups and downs in my life. Also my one year old little Sanuth's lovely smile made me energetic in the most busy year of my studies.

Finally, I would like to thank all of my relatives for their unforgettable encouragements. Many thanks for all of my friends specially who are here with me in Norman, Oklahoma for their support in numerous ways. Though it is not related to this thesis directly, you all made me living much more comfortable as a family even thousands of miles away from our homes. Thanks all for being there.

Table of Contents

List of Tables

List of Figures

Abstract

This dissertation is motivated by two major challenges in modern Physics. One is related to precession measurement and other is related to atmospheric science.

The amount of CP violation (equivalently time reversal (T) symmetry violation) that occurs in the Standard Model, the most successful theory in the particle physics today, is not sufficient to explain why we live in a matter (rather than anti-matter) dominated universe. A measurable electric dipole moment of the electron (e-EDM) proportional to its spin may help to unravel this matter anti-matter mystery and could point the way to physics beyond the Standard Model.

As an e-EDM probe, both cold molecular trap and molecular beam techniques have been proposed. In this thesis we show that the geometric phase effect limits the viability of a cold molecular trap technique. Specifically we show the molecular trap method can not be employed for PbF until the technology is available to cool down molecules to ultra cold temperatures.

This thesis also addresses two major difficulties that need to be overcome in order to carry out a molecular beam e-EDM measurement. One of these difficulties is that background magnetic fields mimic the e-EDM. For this reason, molecules with small magnetic g-factors greatly reduce the background due to this effect. In this dissertation investigation of the Zeeman structure of the PbF molecule including state dependent g-factor measurements are determined through extensive analysis of microwave spectroscopy.

The other major difficulty addressed in this thesis is the requirement to create a

highly uniform electric field that can be reversed in a precise and consistent manner. Specifically we describe a precise high voltage control and switching system that has been built.

Isotopic detection of Krypton has many important applications including archaeological dating beyond that possible using ^{14}C and nuclear activity monitoring all around the world. It has been shown that laser cooling and trapping of metastable Kr ($5s[3/2]_2$) is an effective means to achieve detection efficiencies of 1 part in 10^{12}. A limiting factor in these studies is the production of metastable Kr, which is currently implemented using an RF discharge. In this dissertation, an attempt at laser-based excitation is described which may be useful to increase these detection efficiencies by many orders of magnitude.

Chapter 1

Introduction

This work is motivated by two different areas of physics. Precession measurement and atmospheric science. In a precession measurement experiment, we are dedicated to measuring the electron electric dipole moment (e-EDM) using the PbF molecule. The motivation and a brief introduction to the Physics related this experiment can be found in sections 1.1 and 1.2. The progress has been made towards this measurement can be found in section 1.3.

In an experiment that has direct applications in atmospheric science, this thesis describes an attempt at optical production of metastable Kr. Details of this attempt, can be found in Chapter 5.

1.1 Electron electric dipole moment and CP violation

More than half a century ago, in 1950 E.M. Purcell and N.F. Ramsey suggested that the electron might have an electric dipole moment proportional to its spin [14]. Existence of such an electric dipole moment would break the time reversal symmetry (T) and would imply charge conjugation (C-interchange of particles and anti-particles) and parity (P-space inversion) violating physics, namely CP violation. According to the most successful theory in particle physics today, the Standard Model CP violation is somewhat allowed. However, it is not sufficient to explain some mysteries in the Universe. These mysteries include the matter-antimatter asymmetry, dark energy,

and masses of quarks and leptons.Hence, searching for e-EDM means searching for new physics.

In order to realize the statement that e-EDM violates CP-symmetry we consider the energy of an electron due to the coupling between its angular momenta proportional to spin (magnetic dipole moment-$\vec{m}$ and assuming an electric dipole moment-$\vec{p_e}$) and the external fields. The resulting energy can be written as,

$$U = -\vec{p_e} \cdot \vec{E} - \vec{m} \cdot \vec{B} \tag{1.1}$$

where, $\vec{p_e} = -g_{edm}\mu_B\vec{S}$ and $\vec{m} = -g\mu_B\vec{S}$ with $g \approx 2$ and $g_{edm} < 10^{-18}$. Here $\mu_B = \frac{|e|\hbar}{2m}$ is the Bohr magneton.

By applying external fields in z-direction such that $\vec{E} = E_o\hat{z}$ and $\vec{B} = B_o\hat{z}$ we find,

$$U = \mu_B \left(g_{edm}E_o + gB_o\right) S_z \tag{1.2}$$

The energy splitting between spin up $S_z = \hbar/2$ and spin down $S_z = -\hbar/2$ states can be written as,

$$\Delta U_t = |U_\uparrow - U_\downarrow| = |\mu_B \left(g_{edm}E_o + gB_o\right) \hbar|. \tag{1.3}$$

Upon time reversal ($t \to -t$) spin and B-field flip the sign. so, we get

$$\Delta U_{-t} = |U_\uparrow - U_\downarrow| = |\mu_B \left(-g_{edm}E_o + gB_o\right) \hbar| \neq \Delta U_t. \tag{1.4}$$

Eq. 1.4 indicates that to resonantly excite the system from its ground state to its excited state requires a photon frequency that depends on the direction of time. As such, existence of an e-EDM breaks time reversal symmetry.

CPT symmetry (symmetry upon reversal of charge, parity, and time) is steeped in the physics of Lorentz symmetry and causality [15]. As such it is viewed as far

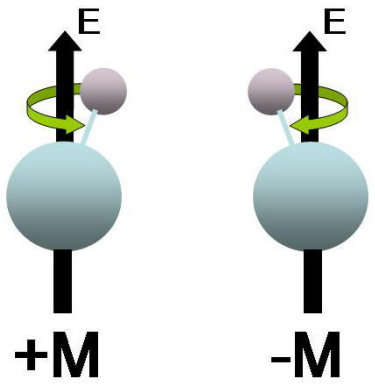

Figure 1.1: Degeneracy lifting of $\pm M$ states due to e-EDM

more fundamental than any individual (C, P, or T) symmetry. For this reason, if one accepts CPT symmetry then T violation is equivalent to CP violation. Therefore, the existence of e-EDM proportional to spin is often quoted as CP violation. According to the current and leading theory of particle physics, the Standard Model, prediction of electric dipole moment of the electron is less than 10^{-38} e·cm. However, Super Symmetry, a theory beyond the Standard Model predicts a value between $10^{-27} - 10^{-32}$ e·cm which may be reached by our on going experimental efforts.

1.2 e-EDM searches using atoms and molecules

Time reversal symmetry (T) leads to a degeneracy of two states of any atom or molecule that differ only by the sign of the projection (M) of total angular momentum (F) onto the axis of a pure electric field. Existence of an e-EDM would lift this degeneracy.

Until very recently, the limit of the e-EDM was known from an experiment that determined the energy splitting between M=1 and M=-1 states of Tl 6 $^2\mathrm{p}_{\frac{1}{2}}$(F=1)

atoms in a 100 kV/cm field that is parallel and anti-parallel to a magnetic field of order ∼1 G [16]. As a result an experimental upper bound of 1.6×10^{-27} e·cm for e-EDM has been placed. Heavy polar diatomic molecules are 1000 to 10 000 times more sensitive to the e-EDM than atoms due to strong internal electric fields. For example, once it is polarized, valance electron of the PbF molecule feels $\sim 10^{10}$ V/cm effective electric field (E_{eff}) inside the molecule by applying a polarization field ∼ 6 KV/cm [17]. This advantage was finally realized in the 2011 measurement of e-EDM using YbF molecules by placing a new upper bound of 1.05×10^{-27} e·cm by the Hind's group [18]. Today many groups are attempting to improve the limit on e-EDM or to find it using different molecules including us (Cornell - Hf^+ [19], Leanhardt - WC [20], Gabrielse - ThO [21], DeMille - PbO [22], Shafer-Ray - PbF [23]).

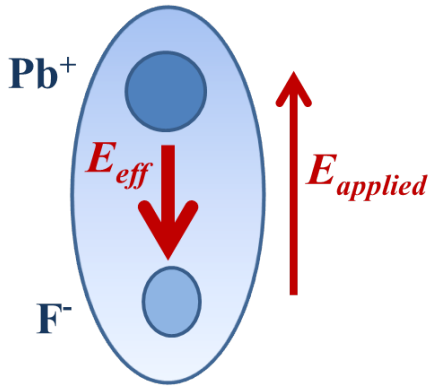

Figure 1.2: Polarized PbF molecule by the laboratory field $E_{applied}$.

For a valance electron in an atom or molecule this splitting is due to spin up and spin down states. Similar to the Eq. 1.3, such a splitting for valence electron in both electric and magnetic fields can be written as

$$\Delta U = |\mu_B \left(g_{edm} E_{eff} + g(E_o) B_o\right) \hbar|. \tag{1.5}$$

We see that Eq. 1.3 becomes Eq. 1.5 as $E_o \rightarrow E_{eff}$ and $g \rightarrow g_{(E_o)}$. As mentioned before, this E_{eff} can be larger than laboratory electric field (E_o) by many orders of magnitude due to the internal enhancement. $g(E_o)$ is the electric field dependent magnetic g-factor. Unlike for a free electron ($g \approx 2$) a valance electron feels a completely different magnetic environment which depends on applied electric field. Due to this reason g-factors close to zero is possible in molecules and greatly improve the sensitivity to the e-EDM. For PbF, $g(6$ kV/cm$) \approx 0.04$. According to Eq. 1.5, it is no surprise that molecules are highly interested candidates in order to improve the current limit of e-EDM.

Table 1.1: Comparison of properties of e-EDM sensitive molecules. "$g-2$" implies g-factor of $\sim$ 0.04 and "g" implies g-factor of $\sim$ 1. (*Ref.[1], **Ref.[2], ***Ref.[3], $^{+}$Ref.[4], $^{++}$Ref.[5], $^{+++}$Ref.[6])

Molecule	**E_{eff}(GV/cm)**	**g-factor magnitude**	**Radiative lifetime (ms)**	**polarization field (kV/cm)**
YbF	32*	g	-	10^{+++}
HgF	95*	g	-	
PbO	23*	g	0.1**	6
ThO	60^{+}	g-2	1.0*	~ 0.0001*
WC	-60^{++}	g-2	-	$\sim 0.001^{++}$
^{206,208}PbF	-31*	g-2	-	6
^{207}PbF	-31*	g-2	-	0.2-1.0
HfF^{+}	30*	g-2	> 200*	0.001-0.1***

1.3 Progress towards measuring e-EDM using PbF molecule

The PbF molecule provides for a 1000-10,000 times improvement in sensitivity to an electron electric dipole moment over atomic based measurements. The large dipole moment, strong internal electric field, and small sensitivity to external magnetic field has made this molecule a leading candidate for the measurement of electron electric dipole moment.

There are two ways one could imagine an e-EDM experiment using gas phase molecules. The first is by probing molecules in a molecular trap and the second is by probing molecules in a molecular beam. For PbF, we show that the trap method can not be employed using current technology due to a geometric phase effect. Trap experiments may be possible whenever technology is available for cool down molecules to ultra cold temperatures. Theoretical and numerical studies which brought us to this conclusion can be found in chapter 2. However, the beam method can be employed and detailed description of our beam source can be found elsewhere [24].

Due to many degrees of freedom, it is hard to create a ground state molecular beam. In other words, population of the ground state molecules is limited. In order to partially overcome this problem supersonic expansion can be used to lower the rotational temperature. However, in order to achieve higher collection rates a sensitive detection method must be implemented. We started many years ago by doing laser spectroscopy in order to understand the molecule. We decided to use resonance enhanced multi-photon ionization (REMPI) as our detection method because it is more sensitive than light induced florescence (LIF) by many orders of magnitude.

As a beginning of this long journey, the ionization scheme, X_1 + hc/(280 nm) → B + hc/(355 nm) → PbF^+ has been tested by using a 10Hz, 10ns, Nd:YAG pumped dye laser. In this experiment we were able to achieve vibrational resolution but the rotational levels could not be resolved [25]. Resolution was limited by the B-state lifetime.

As the next step, the ionization scheme, X_1 + hc/(436 nm) → A + hc/(476 nm) → D + hc/(532 nm) → PbF^+ has been tested by using the same Nd:YAG laser pumped two dye lasers. In this experiment we were able to achieve rotational state resolution but hyperfine states could not be resolved [26].

In order to achieve hyperfine state resolution one of the dye laser was seeded by a diode laser. As a result, hyperfine structure due to the ^{207}Pb was resolved [27]. The ultimate resolution of 10 Hz, 10 ns pulsed dye laser system was limited to 500 MHz and it was not sufficient to resolve hyperfine structure due to ^{19}F which requires about 50 MHz resolution. In order to overcome this problem a new type of detection system was needed. As a result, pc-REMPI was developed.

In pc-REMPI detection method, we used diode laser radiation to excite PbF molecules from the ground X_1 state to the excited A state. Then, an OPO system pumped by 6 ps, 76 MHz Nd:YVO_4 laser radiation (high-Q laser) was used to further excitation and ionization. Specifically, we employed the ionization scheme, X_1 + hc/(436 nm) → A + hc/(476 nm) → D + hc/(476 nm) → PbF^+. Using this new technique pc-REMPI, a much higher data collection duty cycle (≈ 1) was possible compared to 10^{-4} in previous system. Also in this method we replaced our ion detector

with coincidence detector which allows us to detect both ions and the electrons at the same time. As a result, we were able to resolve hyperfine structure due to ^{19}F nucleus [28]. Hyperfine spectrum of PbF was analyzed and lines predicted to ~ 1 MHz accuracy. Electric dipole moment measurements of both X_1 and A states were also carried out. Finally, collaborating with Jens Uwe Grabow of the University of Hannover we were able to determine X_1 state energy levels to roughly 1 part in 10^8 (300 Hz) accuracy by analyzing pure rotational spectra of the X_1 ground state produced by a Fourier transform microwave spectrometer (FTMW) located at Hanover, Germany. Zeeman structure at earth's magnetic field was also analyzed and magnetic g-factors for the molecule has been measured. Detailed description about this measurement can be found in chapter 4. As a result of this collaboration a precise characterization of the ground X_1 state of PbF has been published [8, 29].

As of today we know all the spectroscopic information about the molecule that required to design an e-EDM experiment. We are well on our way to completing the apparatus and electronics in order to carry out our envisioned e-EDM experiment (More detailed description of such an experiment is not a part of this thesis but can be found elsewhere [16, 18].) In this regard, chapter 3 describes our high voltage control and switching system which is dedicated to control the electric field switching required in e-EDM experiment. In order to employ Ramsey beam technique required in this experiment the first generation of Ramsey cavity has been built and tested. Now, all the tools are ready, it's time for the real hunt.

Chapter 2

Effect of the geometric phase on the possible measurement of the electrons electric dipole moment using molecules confined by a Stark gravitational trap

Most of the content presented here appear in Physical Review A, Vol. 78, 033427, 2008.

2.1 Introduction

The possibility that a particle may couple to an external field through an electric dipole moment proportional to spin was first suggested by Purcell and Ramsey[30]. This possibility has led to a search for the electric dipole moment of elementary particles that is still ongoing[31]. The current limit on the electron electric dipole moment ($e-$EDM) has been determined using a Ramsey beam resonance probe of ($^2P_{1/2}$, $F = 1$)Tl atoms[32]. (Here F gives the total angular momentum of the atom.) Specifically, limits on the $e-$EDM have been deduced from the difference between the energy separation of Tl states differing only by the sign of the projection of angular momentum m_F onto a strong electric field axis as the atoms move through a weak magnetic field that is alternately parallel and antiparallel to the electric field[32, 33]. The next generation of $e-$EDM measurements may occur using heavy polar molecules[34, 35, 36]. These molecules afford a roughly 1000 times increase in intrinsic sensitivity over atoms. However it is difficult to create an intense beam

of ground-state polar molecules. For this reason, only very recently have molecular beam experiments become competitive with atomic measurements[37].

The measurement time in Ramsey beam resonance experiment is limited to the $\tau_b \approx 1.0$ ms flight time of the probed particles as they pass through a Ramsey cavity. The sensitivity of such an experiment is greatly improved by the high throughput of particles through the apparatus, leading to a sensitivity to an electric dipole moment that scales as

$$s_{beam} = 1/(\tau_b \sqrt{f_b\, t_{\rm exp}}). \tag{2.1}$$

Here f_b is the rate measurements and $t_{\rm exp}$ is the lifetime of the experiment. For atomic beam experiments, f_b may exceed 10 MHz. For molecular beams, such high data collection rates are more difficult to achieve. One way in which this difficulty maybe overcome is to replace the Ramsey beam resonance method with a trapped molecule experiment. It is notable that efforts to cool and trap molecules have been at least partially justified by the possibility of carrying out just such a precision measurement[34, 38, 39, 40, 41]. In a trapped-molecule measurement, a handful of (or single) molecule is confined to a region of space created by nonuniform electromagnetic fields. The density of molecules must be kept low enough to create a long trap lifetime and the possibility of a long coherence time τ. In the limit of just one molecule in the trap during each of a series of measurements taking a time τ, the number of measurements will scale as $N = t_{\rm exp}/\tau$ and one could expect an $e-$EDM sensitivity that scales as

$$s_{trap} = 1/\sqrt{\tau\, t_{\rm exp}}. \tag{2.2}$$

Setting $s_{trap} = s_{beam}$, one finds that the payoff for creating a trapped experiment occurs when

$$\tau \approx \tau_b^2 f_b. \tag{2.3}$$

Clearly the decision to create a trapped-molecule or beam-resonance experiment depends greatly on the achievable flight time and data collection rate in of a beam-resonance experiment. For example, to achieve an equivalent experimental sensitivity as a Ramsey beam experiment with a collection rate of $f_b = 1$ MHz and flight time $\tau_b = 1$ ms, a trapped-molecule experiment would require a coherence time of $\tau \approx 1$ sec. In this work we make no attempt to estimate what values of τ_b or f_b might be achievable in a molecular beam experiment. Instead we concentrate on limits to the possible value of τ that may be achieved in a trapped molecule experiment.

The coherence time τ for an $e-$EDM experiment is likely to be much shorter than the total time the molecule remains confined to a trap. Here we consider the case of an $e-$EDM measurement taking place in a Stark-gravitational trap and show that milli-K temperatures may be required to achieve a coherence time on the order of seconds for trapped PbF molecules.

2.2 Geometric phase effect relevant to e-EDM experiment

The geometric phase effect that is relevant to the e-EDM experiment occurs in the adiabatic approximation that separates the internal and center of mass motion of a molecule. In order to derive a Hamiltonian that describes the geometric phase effect shown in Eq. 2.4 we use the methodology that Longuet-Higgins[42] applied in the

separation of electronic and nuclear motion in the bohn-oppenheimer approximation. The detailed derivation of this Hamiltonian can be found in our original publication[43].

$$\Omega_{geo}(\vec{r}) = \frac{2m_i\hbar i}{M}\sum_{n=1}^{3}\left[\left(\left(\nabla_n\frac{\vec{e}}{e}\right)\times\frac{\vec{e}}{e}\right)\cdot\hat{z}\right]\nabla_n \tag{2.4}$$

Here $\vec{e}$ is the sum of the laboratory frame electric field vector and the direction of the laboratory-frame quantization axis

$$\vec{e} = \widehat{\mathcal{E}}\,(\vec{r}) + \hat{z}. \tag{2.5}$$

In order to gain some insight into the geometric interaction of Eq 2.4, it is useful to consider the classical case for which $(-i\hbar\vec{\nabla})$ becomes $M\vec{v}$ where $\vec{v}$ is the velocity of the center of mass. In this case we have

$$\Omega_{geo}(\vec{r})\ (\text{classical}) = -\frac{2m_i}{e^2}\left(\left(\frac{d}{dt}\vec{e}\right)\times\vec{e}\right)\cdot\hat{z}. \tag{2.6}$$

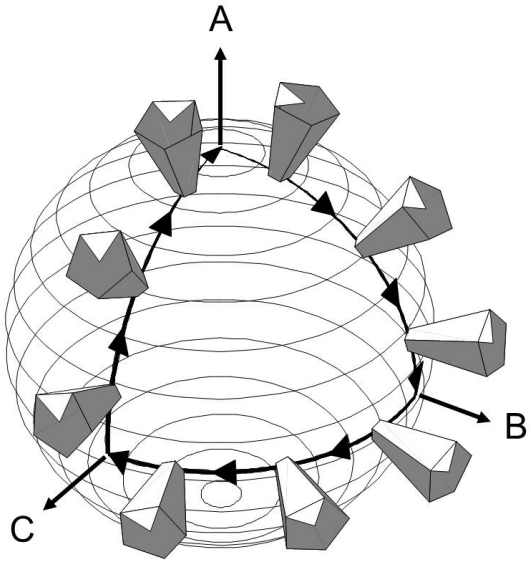

Figure 2.1: Graphical illustration of the geometric phase effect.

Fig. 2.1 gives a geometric picture of the geometric phase effect. Here a unit sphere gives a representation of the direction $\widehat{\mathcal{E}}$ of the electric field vector whereas the orientation of the white side of the polyhedron gives a graphical representation of the relative phase between a coherent superposition of $\pm m_F$ states. (This graphical representation can be put on solid theoretical ground by considering the spherical tensor moments that describe the angular momentum distribution[44].) The figure illustrates the physical phase accumulation as the electric field rotates from orientation A to B to C and back again to A. One can see that when the system returns to its original orientation A, a geometric phase of $-\pi/2$ is accumulated.

It is helpful to see how the $A \rightarrow B \rightarrow C \rightarrow A$ transformation of Fig. 2.1 is described in terms of a fixed coordinate system and Eq 2.6. First we suppose that $\hat{z} = \hat{A}$. Fig. 2.1 illustrates that as the system evolves along the $A \rightarrow B$ path, the orientation of the fixed frame wave function does not change. The fact that the wave function is stationary is predicted by Eq 2.6: Along this transformation from A to B the vectors $\vec{e}$, $d\vec{e}/dt$ and $\hat{z} = \hat{A}$ are all in the same plane so $\Omega_{geo} = 0$. Along the path from B to C, the fixed-frame wave function undergoes a rotation of $-\pi/2$. Here $d\vec{e}/dt = -\omega_{rot}\hat{A} \times \vec{e}$ and $\Omega_{geo} = -m_i\omega_{rot}$, causing a total geometric angle $\Theta_i = -m_i\pi/2$ to accumulate over the path. Along the path from C back to A the vectors $\vec{e}$, $d\vec{e}/dt$ and $\hat{A} = \hat{z}$ are again in a single plane and $\Omega_{geo} = 0$. Thus the total round-trip phase accumulation is $\Theta_i = -m_i\pi/2$. This is exactly the phase required to rotate the spherical tensor moments describing the initial state through an angle $-\pi/2$.

Let us reconsider the same $A \rightarrow B \rightarrow C \rightarrow A$ transformation, but this time

taking $\hat{z} = \hat{B}$. For this case $\Omega_{geo} = 0$ for the first and second transformations and $\Omega_{geo} = -m_i\omega_{rot}$ for the final $C \rightarrow A$ transformation. Again the round-trip phase accumulation is given by $\Theta_i = -m_i\pi/2$. The fact that Ω_{geo} depends on $\hat{z}$ is an artifact of our choice of quantization axis. The wave function itself evolves in a manner that is independent of the choice of coordinate system.

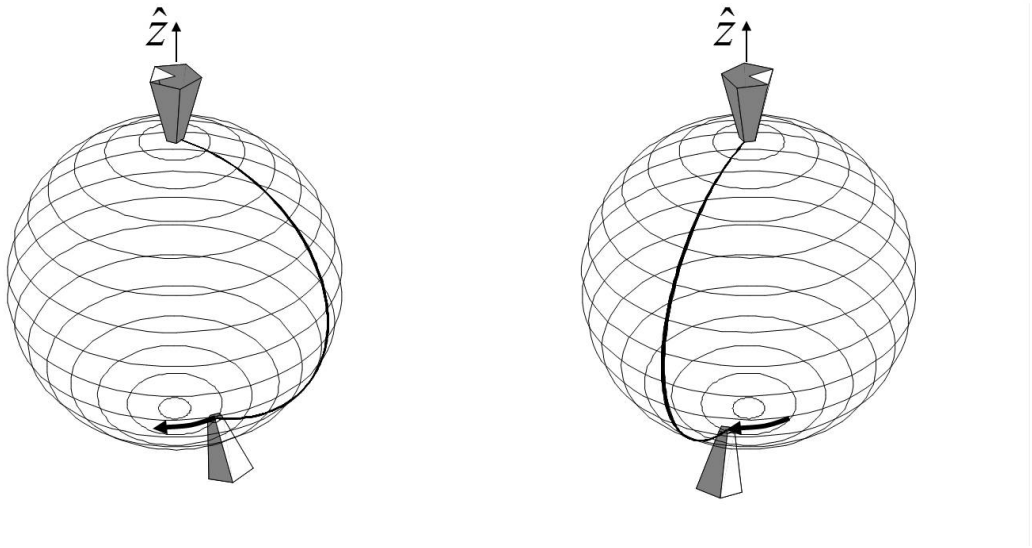

Figure 2.2: Graphical illustration of the divergence in Ω_{geo} as $\widehat{\mathcal{E}}$ approaches $-\hat{z}$.

The observant reader may be bothered by the fact that $\Omega_{geo}(\vec{r})$ becomes infinite at $\widehat{\mathcal{E}}(\vec{r}) = -\hat{z}$. An intuition for the source of this infinity can be gained by from the illustration of the geometric phase effect over a small rotation of $\widehat{\mathcal{E}}$ in the region of $-\hat{z}$ that is shown in Fig. 2.2. Note that as the initial orientation the electric field approaches $-\hat{z}$, an infinitesimal change in $\widehat{\mathcal{E}}(\vec{r})$ leads to a finite change in the phase of the basis set functions orientation. If we assume this orientation corresponds to the phase of a coherent superposition of $\pm m_F$ states, we see that this sensitivity will require an infinite rate of change Ω_{geo} as $\widehat{\mathcal{E}}(\vec{r})$ crosses $-\hat{z}$.

If one starts from a quantum mechanical picture, one expects energy perturbations due to the geometric phase effect that are given by the expectation value of the term of Eq 2.4. In a classical picture, one expects a phase that competes with an $e-$EDM signal to accumulate at a rate given by the interaction of Eq 2.6. The next section introduces a model system in order to illustrate the application of these terms to predict the effect of the geometric phase on an $e-$EDM measurement.

2.3 The Stark gravitational trap

In a previous work[45], we showed that it is possible to create a static electric field with a local minimum in its magnitude at a location in space where $\vec{\mathcal{E}} \neq \vec{0}$. We have also shown that this is possible in three dimensions, but not in a two dimensional guide[46]. In addition, we have demonstrated specific electrode configurations to create electric fields with this property. Molecules in quantum states with a Stark energy $U(\mathcal{E})$ that increases with increasing field strength that are placed at a point of minimum magnitude $\mathcal{E}$ will experience a confining potential. Here we consider a different trap design then we considered previously. Specifically we consider a Stark-gravitational trap, largely because its potential has a simple analytic form which in turn simplifies our analysis. For this trap, molecules are confined by the potential

$$U_{trap}(\vec{r}) = U(\mathcal{E}) + Mg_r x - U(\mathcal{E}_o) \tag{2.7}$$

$$\approx U' \frac{(\mathcal{E} - \mathcal{E}_o)}{\mathcal{E}_o} + Mg_r x \tag{2.8}$$

where

$$U' = \mathcal{E}_o \left. \frac{dU}{d\mathcal{E}} \right|_{\mathcal{E}_o} \tag{2.9}$$

and $\vec{\mathcal{E}} = -\vec{\nabla} V$ with

$$V(x, y, z) = -\mathcal{E}_o (z - \frac{xz}{h_g} + \frac{3r^2 z - 5z^3}{18 h_g^2}). \tag{2.10}$$

Here $\vec{g}_r = -9.8$ m/s^2 $\hat{x}$ is the acceleration due to gravity. (A subscript has been added to avoid confusion with the magnetic g factor.) The parameter $\vec{\mathcal{E}}_o = \mathcal{E}_o \hat{z}$ is the electric field at the center of the trap. The only other adjustable parameter is the length h_g which may be controlled by the curvature of the trap plates. If we set h_g equal to the ratio of U' to the molecules weight,

$$h_g = U'/M g_r, \tag{2.11}$$

then trap potential of Eq 2.7 becomes isotropic to order r^3:

$$U_{\text{trap}} = \frac{1}{2} M \left(\frac{g_r}{3 h_g} \right) r^2 + O[(\frac{r}{h_g})^3]. \tag{2.12}$$

We note that the choice to make the trap isotropic to order r^3 is some what arbitrary. However, this choice allows for a simple analytic approximation for the center-of-mass motion and is therefore appropriate for this general discussion. For the case of PbF in its ground state, the parameter h_g is on the order of 10 cm and the trap frequency $\omega/2\pi$ is approximately 1 Hz.

The electric potential $V(x, y, z)$ can be created from two plates held at equipotential surfaces of $\pm V_{\text{plate}}$. Letting

$$\alpha = \frac{9}{2} \frac{V_{\text{plate}}}{\mathcal{E}_o h_g} \tag{2.13}$$

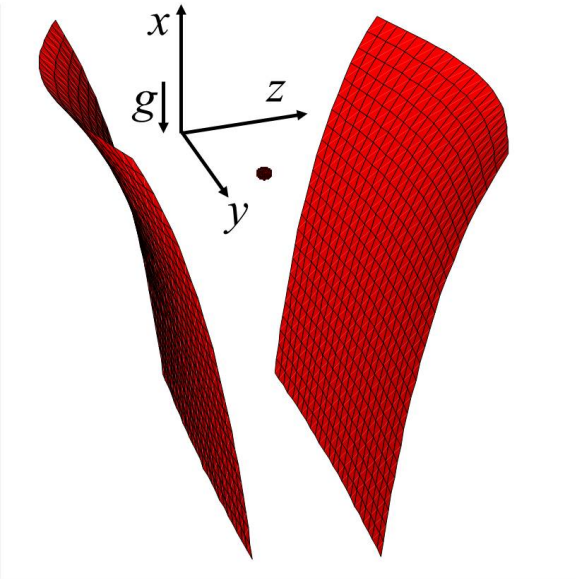

Figure 2.3: Visualization of molecules confined by a Stark-gravitational trap.

and

$$h_{xy} = 3h_g - 3x + \frac{x^2 + y^2}{2h_g} \tag{2.14}$$

then the curvature of the two plates is defined by the equipotential surfaces

$$z_{\pm} = \pm 2h_{xy} \cos\left(\frac{1}{3}\arccos(\alpha\ (h_{xy}/h_g)^3) - \frac{2\pi}{3}\right). \tag{2.15}$$

A visualization of molecules trapped between plates of this curvature is shown in Fig. 2.3.

2.4 Geometric phase induced limit on coherence time

By considering isotropic three-dimensional harmonic motion in the trap, it can be shown that the quantum mechanical phase accumulation between $\pm m_F$ states due to

the geometric phase effect as,

$$\begin{aligned}\Delta\omega_{m_F} &= \frac{\omega}{12}\sqrt{\frac{5}{2}}\frac{\Delta m_F}{U'^2}\left[\frac{\sum_n \frac{(n+1)(n+2)}{2}\left(E_n^2-\frac{9}{4}\hbar^2\omega^2\right)\left(E_n^2-\frac{77}{20}\hbar^2\omega^2\right)e^{-\hbar\omega(n+\frac{3}{2})/k_BT}}{\sum_n \frac{(n+1)(n+2)}{2}e^{-\hbar\omega(n+\frac{3}{2})/k_BT}}\right]^{1/2} \\ &= \frac{5}{2}\Delta m_F\,\omega\left[\frac{T}{T'}\right]^2\left[\sqrt{\frac{21+4\cosh\frac{\hbar\omega}{k_BT}}{25}}\left(\frac{\frac{\hbar\omega}{2k_BT}}{\sinh\frac{\hbar\omega}{2k_BT}}\right)^2\right] \qquad (2.16)\end{aligned}$$

where, $E_n = \hbar\omega\left(n+\frac{3}{2}\right)$.

Detailed derivation of this result can also be found in the original publication[43]. Classical picture of Eq. 2.16 can be obtained by considering the limit $\hbar \to 0$. This result shows that the phase accumulation is proportional to the trap loading temperature squared.

$$\Delta\omega_{m_F} = \frac{5}{2}\Delta m_F\,\omega\left[\frac{T}{T'}\right]^2\left[1+O[\left(\frac{\hbar\omega}{k_BT}\right)^2]\right] \qquad (2.17)$$

The geometric phase limited coherence time can be obtained as,

$$\tau = \frac{2\pi}{\Delta\omega_{m_F}} \qquad (2.18)$$

2.5 Semiclassical Trajectory Calculation of the Coherence Time in a Stark Gravitational Strap

To move from a quantum to a semiclassical derivation of $\Delta\omega_{m_F}$, we change our picture of loading the trap in a harmonic state n and geometric phase state k to a picture of loading the trap with an initial velocity $\vec{v}_k$ at a position $\vec{r}_k$. The resulting time-dependent trajectory $\vec{r}_k(t)$ leads to a time-dependent rate of phase change $\delta\omega_{m_F,k}(t)$ given by

$$\delta\omega_{m_F,k}(t) = 2m_F\left(\frac{1}{\hbar}g(\mathcal{E})\mu_B\vec{B}\cdot\widehat{\mathcal{E}} + \frac{2}{e^2}(\vec{v}_k(t)\cdot\vec{\nabla}\vec{e})\times\vec{e}\cdot\hat{z}\right). \qquad (2.19)$$

Here $\vec{\mathcal{E}} = \vec{\mathcal{E}}(\vec{r}_k(t))$, μ_B is the Bohr magneton and $\vec{e}$ is given by Eq 2.5. Finally $g(\mathcal{E})$ is the field dependent $g-$factor . In this work assume a constant background field $\vec{B} = B_x\hat{x} + B_y\hat{y} + B_z\hat{j}$ as well as more general case of a spatially dependent magnetic field.

We note that the dependence of $\delta\omega_{m_F,k}(t)$ on the dot product $\vec{B} \cdot \widehat{\mathcal{E}}$ is not CP violating. Instead the dependence on the product is a result of the initial polarization of the molecule with respect to the $\widehat{\mathcal{E}}$ axis and the assumed adiabatic motion of the molecule. The mean value of $\delta\omega_{m_F,k}(t)$ during a measurement gives our semiclassical approximation of $\delta\omega_{m_F,k}$:

$$\delta\omega_{m_F,k} = \frac{1}{t}\int_0^t \delta\omega_{m_F,k}(t')dt'. \tag{2.20}$$

A numerical simulation is carried out to numerically evaluate the integral of Eq 2.20 for values of $\vec{v}_k$ and $\vec{r}_k$ chosen randomly from a thermal distribution For each simulation, the value of t is taken to be large enough for $\delta\omega_{m_F,k}$ to converge to a constant value. For some of the simulations we run, we assume the harmonic approximation

$$\vec{r}_k(t) = (A_x\cos(\omega t + \phi_x), A_y\cos(\omega t + \phi_y), A_z\cos(\omega t + \phi_z)) \tag{2.21}$$

where $A_x, A_y, A_z, \phi_x, \phi_y$, and ϕ_z are taken from the distribution

$$P(A_x, A_y, A_z, \phi_x, \phi_y, \phi_z) = \frac{A_x A_y A_z}{(2\pi)^3 A_o^6} e^{-(A_x^2+A_y^2+A_z^2)/2A_o^2} \tag{2.22}$$

with

$$A_o = \left[\frac{k_B T}{M\omega^2}\right]^{1/2}. \tag{2.23}$$

Because we consider the effect of a background electric field, the mean value of $\delta\omega_{m_F,k}$ averaged over a large number N of trajectories,

$$\delta\bar{\omega}_{m_F} = \frac{1}{N}\sum_k \delta\omega_{m_F,k}, \tag{2.24}$$

does not necessarily vanish. The coherence time τ is determined by the standard deviation of $\delta\omega_{m_F,k}$ from this mean value:

$$\Delta\omega_{m_F} = \frac{1}{\tau} = \sqrt{\frac{1}{N}\sum_i (\delta\omega_{m_F,k} - \delta\bar{\omega}_{m_F})^2}. \tag{2.25}$$

For the purely isotropic harmonic trajectory of Eq 2.21, the expected values of $\delta\bar{\omega}_{m_F}$ and $\Delta\omega_{m_F}$ can be calculated analytically to a given order in T/T'. Specifically, one can show

$$\delta\bar{\omega}_{m_F} = \mu_B \left(g - \frac{3}{2}(g - g' - g'')\frac{T}{T'} + O[(\frac{T}{T'})^2] \right) \vec{B}\cdot\hat{z} \tag{2.26}$$

and

$$\begin{aligned}\Delta\omega_{m_F}^2 = {} & \Delta m_F^2 \left[\frac{5}{2}\omega\right]^2 \left[\left(\frac{T}{T'}\right)^4 + O\left[\left(\frac{T}{T'}\right)^5\right]\right] \\ & + \Delta m_F^2 \frac{\mu_B^2}{\hbar^2}\left[\frac{1}{2}g^2 B_y^2 + \frac{1}{2}(2g - 3g')^2 B_x^2 + \frac{3}{4}(3g^2 - 2gg' + g'^2 + 2g'g'' + 3g''^2)B_z^2\right] \times \\ & \left[\left(\frac{T}{T'}\right)^2 + O\left[\left(\frac{T}{T'}\right)^3\right]\right].\end{aligned} \tag{2.27}$$

Here g, g' and g'' are defined in Table 1. A comparison of this analytical result for $\Delta\omega_{m_F}$ to numerical simulation is given in Fig. 2.4, Fig. 2.5 and Fig. 2.6. For the case $\vec{B} = \vec{0}$, Eq 2.27 agrees with Eq 2.17 as $\hbar \to 0$.

Recall that U' is the product of the derivative of the Stark potential with respect to electric field and the electric field at the trap center (Eq 2.9.) From the result

of Eq 2.27 we see that the temperature $T' = U'/k_B$ dictates the behavior of the experiment. For the case that the loading temperature is approximately equal to T', the inverse of the coherence time will be on the order quadratic sum of the harmonic frequency of the trap and the Zeeman split due to the background magnetic field. As the load temperature becomes colder than T', the contribution proportional to the trap frequency (caused by the geometric phase effect) will fall off quadratically, whereas the contribution due to background magnetic fields will fall off linearly.

As a final investigation of the effect of the geometric phase, we consider the contribution of non-harmonic terms in the trap potential of Eq 2.7. To do so, we carry out numerical evaluations of the integral of Eq 2.20, replacing the trajectories of Eq 2.21 with classical trajectories assuming a more realistic potential. Specifically, we begin with a third-order expansion of $U(\mathcal{E})$ about the trap field $\mathcal{E}_o$:

$$U_{trap}(\mathcal{E}) \approx U' \left(\frac{\mathcal{E}-\mathcal{E}_o}{\mathcal{E}_o}\right) + \frac{1}{2!}U'' \left(\frac{\mathcal{E}-\mathcal{E}_o}{\mathcal{E}_o}\right)^2 + \frac{1}{3!}U''' \left(\frac{\mathcal{E}-\mathcal{E}_o}{\mathcal{E}_o}\right)^3 + Mg_r x \quad (2.28)$$

Parameters that enter this numerical calculation are the acceleration of gravity g_r, the mass of the molecule, the value of $|m_F|$, the value of the background magnetic field $\vec{B}$, and the values of U', U'', U'', g, g', and g'', which describe the value of the Stark and Zeeman interaction in the trap. These values are listed in the table. For these parameters the temperature $T' = U'/k_B = 27.3$ mK and the trap frequency $\omega = \sqrt{Mg_r^2/3U'} = 5.65$ rad/s. The values of U', U'', U'', g, g', and g'' are found by evaluating the eigenvalues of the spin rotational Hamiltonian of the ^{208}Pb^{19}F($X^2\Pi_{1/2}$ v=0) molecule as described by Kozlov et. al[47] and choosing $\mathcal{E}_o$ to be 2.2kV/cm. We note that we consider the lowest-energy low field seeking state with $|m_F| = 1$. This

state is a strong mixture of the $J = 1/2$ and $J = 3/2$ states of the molecule.

Table 2.1: Values of parameters used in the numerical evaluation of $\Delta\omega$

M	$\lvert m_F\rvert$	U'	U''	U'''	g	g'	g''
227u	1	$0.0190\ \mathrm{cm}^{-1}$	$0.00235\mathrm{cm}^{-1}$	$-0.0294\ \mathrm{cm}^{-1}$	0.0890	-0.0318	0.00596
		$\mathcal{E}_o \left.\frac{dU}{d\mathcal{E}}\right\vert_{\mathcal{E}_o}$	$\mathcal{E}_o^2 \left.\frac{d^2U}{d\mathcal{E}^2}\right\vert_{\mathcal{E}_o}$	$\mathcal{E}_o^3 \left.\frac{d^3U}{d\mathcal{E}^3}\right\vert_{\mathcal{E}_o}$	$g(\mathcal{E}_o)$	$\mathcal{E}_o \left.\frac{dg(\mathcal{E})}{d\mathcal{E}}\right\vert_{\mathcal{E}_o}$	$\mathcal{E}_o^2 \left.\frac{d^2g}{d\mathcal{E}^2}\right\vert_{\mathcal{E}_o}$

Figure 2.4 shows the effect of a 100 nG background magnetic field on $\Delta\omega_{m_F}$. (The field is arbitrarily directed so that $\vec{B} = (50.0\hat{\imath} + 70.1\hat{\jmath} + 50.9\hat{k})$nG.) Here the background magnetic field limits the coherence time. In this case, the difference between the coherence time given a harmonic trap (Eq 2.27) and the more realistic trap potential of Eq 2.28 is not dramatic. Figure 2.6 shows a comparison of the effect of the geometric phase given a harmonic trap and the trap potential of Eq 2.28. Here the coherence time is significantly longer than the estimate of the harmonic trap potential. This is not entirely unexpected: The geometric phase couples the angular momentum of molecule with the angular momentum associated with motion of its center of mass. For the angular-momentum-conserving harmonic trap this coupling is enhanced. We note that although the realistic trap potential shows a coherence time that is roughly ten times longer than the harmonic case, for both cases the geometric phase effect limits the coherence time by a factor that is quadratic in temperature. Thus the ultimate temperature that must be reached for a long coherence time in a Stark-gravitational trap is not dramatically different from the analytic prediction given by the harmonic potential.

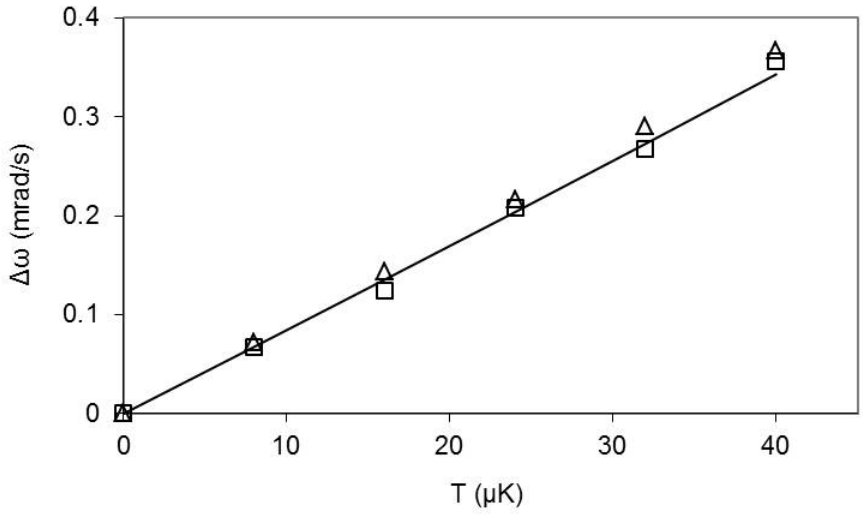

Figure 2.4: Temperature dependence of the inverse of the coherence time ($\Delta\omega_{m_F} = 1/\tau$) assuming a 100 nG magnet field: Solid Line: $\Delta\omega_{m_F}$ determined from Eq 2.27. Triangles: $\Delta\omega_{m_F}$ determined from numerical integration of Eq 2.20 assuming the trajectories of Eq 2.21. Squares: $\Delta\omega_{m_F}$ determined from numerical integration of Eq 2.20 assuming classical trajectories in the potential of Eq.2.28.

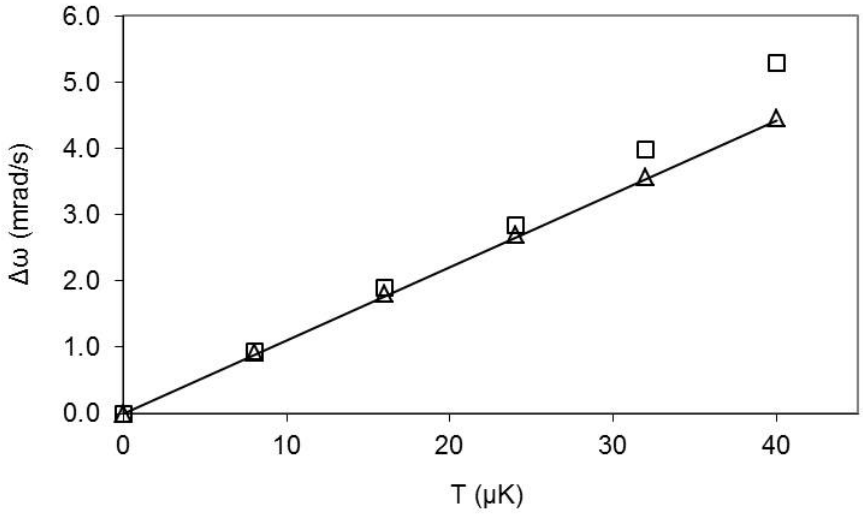

Figure 2.5: Same as Fig. 2.4, but assuming the 1000 nG spatially dependent background magnetic field.

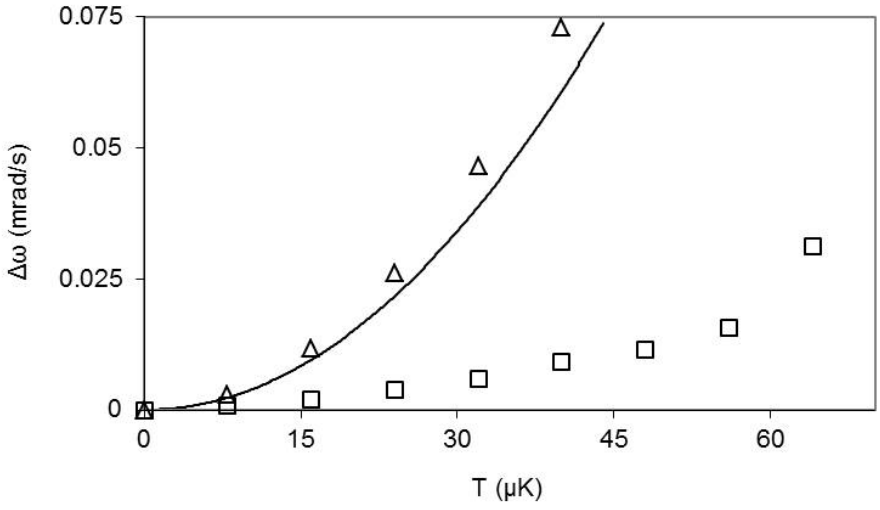

Figure 2.6: Same as Fig. 2.4, but assuming the absence of a background magnetic field.

2.6 Conclusion

Among the list of reasons to create cold molecular species has been the potential to measure the $e-$EDM. In such an experiment, one attempts to measure a coupling of angular momentum to electric field. Such a coupling would break the usual degeneracy of Stark states differing only by the sign of the projection of angular momentum on the electric field axis. One possible way in which cold molecules could be confined for such a measurement is by creating an non-uniform electric field. If such an experiment is carried out, the effect of a geometric phase must be considered. Here we have gone back to the work of Longuet-Higgins in order to derive a simple expression for this geometric interaction that is applicable for both quantum (Eq 2.4) and semiclassical (Eq 2.6) determinations of this effect. We then apply this geometric phase correction to the case of an $e-$EDM measurement and show that the coherence time is expected to scale as the product of the trap frequency and the square of the temperature of the trapped molecules. We use our results to estimate that, for a Stark-gravitational trap to be competitive with a molecular beam experiment, temperatures of roughly 10 milliKelvin or below will be required. As technologies develop to cool molecules to the ultracold regime, the Stark-gravitational trap may provide a useful environment for a sensitive $e-$EDM experiment.

Chapter 3

Designing and building of a high voltage switching control system

3.1 Introduction

Almost all experiment strategies to measure an e-EDM look for a change in the energy splitting between two states only differ by the sign of the projection of the total angular momentum on the quantization axis ($\pm M_F$) for the case of electric field parallel and anti-parallel to an applied magnetic field (see chapter 1). This requires precise and continuous switching of high voltage between positive and negative values: If the E-field magnitudes are not the same before and after the reversal it could cause a severe systematic error in the measurement because the magnetic g-factor is itself a function of electric field. For this reason, an imperfect field reversal may cause a (normal) Zeeman effect to mimic the (exotic) e-EDM effect we seek to measure.

To put this effect on a quantitative footing, consider the fact that an e-EDM of 10^{-27}e.cm (the current limit [18]) leads to an energy difference of 10^{-3} Hz for the $|F = 1, M = \pm 1\rangle$ states of the ground X_1 (J = 1/2) level of the PbF molecule. On the other hand $\frac{dg_{(E)}}{dE}$ at a polarization field of 6 kV/cm is given by $\frac{-0.005}{(kV/cm)}$. These numbers create a tolerance for the error ΔE in the electric field reversal:

$$\frac{dg_E}{dE}\Delta E \mu_B B \leq 10^{-3} Hz. \tag{3.1}$$

If we assume the static B-field is of the order 10^{-5} G, this implies $\Delta E = 14.3$ V/cm and $\frac{\Delta E}{E} \approx 0.2\%$. Thus to measure an e-EDM at the current limit we must control our high

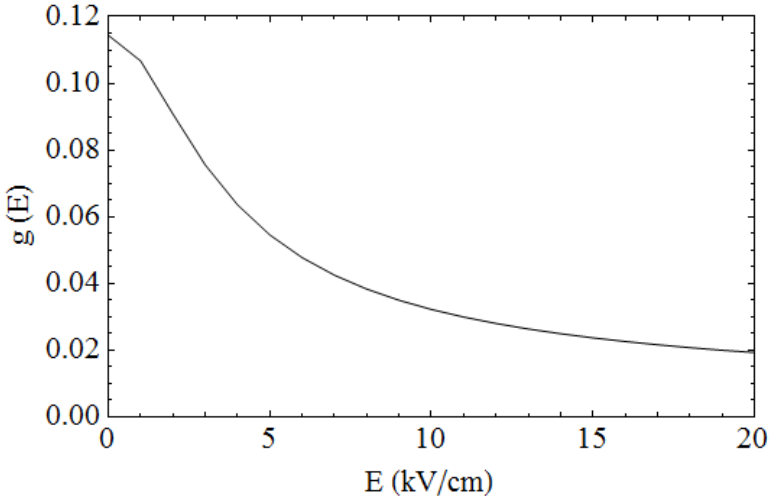

Figure 3.1: Variation of g-factor in the ground state of PbF with the applied electric field [8]

voltage reversal to 0.2%. The best way to overcome this problem is that controlling the high voltage output by controlling a corresponding digital input voltage. Since digital voltages can be repeated with high accuracy, the repeatability of corresponding high voltage output can be controlled precisely through a digital to analog converter. In this chapter we briefly describe a high voltage supply that allows for reversals accurate to better than the ability of our test equipment to measure (0.03%). Details of its construction can be found in Appendices A to D.

3.2 Homemade high voltage control and switching system

Further complicating constraints on our high voltage supply is our choice of resonance enhanced multi-photon ionization (REMPI) detection. Upon reversal of the high voltage in the resonance cavity (drift region in a Ramsey cavity) we must also reverse

high voltages that control polarization, extraction and detector bias voltages. In order to accomplish this task we have built a five channel high voltage control system such that all channels can be reversed simultaneously. These channels are identical but controls high voltages independently except reversal. A main function of a channel is tracking a voltage. This voltage can be input either by using front panel or by using computer remote control. Once reversal is requested channel is capable of lowering the voltage gradually until zero and then tracking back to its original voltage after the reversal. The front panel of the device is shown in Fig. 3.2.

Figure 3.2: The front panel of the high voltage control unit. Numbers appear in displays are in kV

3.3 Conclusion

We have built a five channel reversible high voltage control system that exceeds the 0.2% tolerence achieved by the physics of our e-EDM measurement.

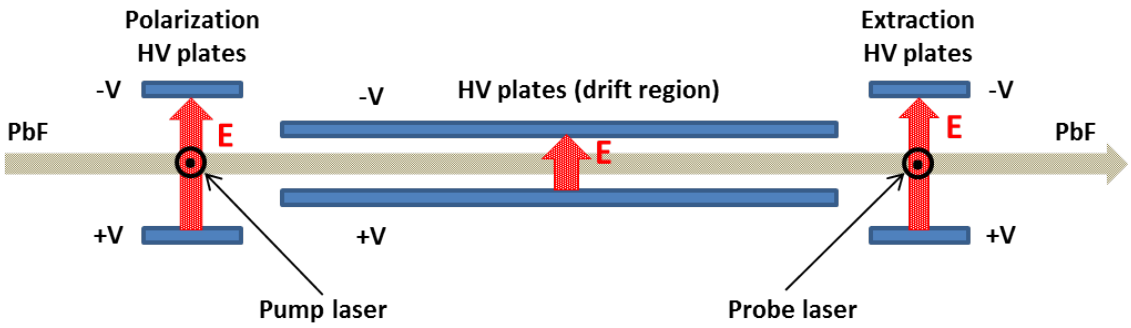

Figure 3.3: High voltage regions used in Ramsey beam e-EDM experiment

Chapter 4

Hyperfine Zeeman structure of the PbF molecule and implications for an e-EDM measurement

4.1 Introduction

In previous chapters of this thesis, our discussion of the interaction of a PbF molecule with external fields has been simplified. A realistic description of interactions of magnetic and electric dipole moments with external fields require introduction of a effective Hamiltonian [8].

$$H = \beta \mathbf{J^2} - \Delta \mathbf{S'} \cdot \mathbf{J} + \mathbf{I} \cdot \widehat{A} \cdot \mathbf{S'} + D\ \mathbf{E} \cdot \widehat{\mathbf{n}} + \mu_B \mathbf{B'} \cdot \widehat{G} \cdot \mathbf{S'} + E_{eff}\ p_e\ \mathbf{S'} \cdot \widehat{\mathbf{n}} \qquad (4.1)$$

The first four interactions describe molecular rotation, spin orbit (Ω doubling), hyperfine, and external electric field interactions. Here, β is the rotational constant, Δ is the fine structure constant, $\widehat{A}$ and $\widehat{G}$ are constant rank one spherical tensors with elements $A^1_0 = A_{||}$, $A^1_{\pm 1} = A_\perp$ and $G^1_0 = G_{||}$, $G^1_{\pm 1} = G_\perp$ respectively, $\mathbf{J}$ is the total angular momentum of the molecule neglecting nuclear spin, $\mathbf{I}$ is the nuclear spin of fluorine nucleus, $\mathbf{S'}$ is the pseudo spin angular momentum, D is the electric dipole moment of the molecule, $\mathbf{E}$ and $\mathbf{B}$ are applied electric and magnetic fields respectively, $\widehat{\mathbf{n}}$ is the direction of the electric field, E_{eff} is the magnitude of effective electric field inside the molecule, p_e is the electric dipole moment of the electron, and μ_B is the Bohr magneton.

By symmetry none of the first four interactions can break the $\pm M_F$ degeneracy of two states that differ only by the sign of the projection of the total angular momentum

(F) on the electric field axis. The last two interactions do, however, lift this degeneracy. The first of these degeneracy lifting interactions, $\mu_B \mathbf{B}' \cdot \widehat{G} \cdot \mathbf{S}'$, is the usual Zeeman interaction. The second is the CP-violating effect of an electron electric dipole moment.

Our experiment relies on the Zeeman interaction being suppressed compared to most molecules. It is not unreasonable to think that this should be the case, the groung state of PbF is $^2\Pi_{1/2}$. Thus naively, 1/2 quanta of spin angular momentum should cancel the magnetic moment of 1 quanta of orbital angular momentum. Indeed, for light molecules such as NO and OH, the magnetic moment of their $^2\Pi_{1/2}$ states is very nearly $g - 2$. Unfortunately, $^2\Pi_{1/2}$ states are strongly mixed with $^2\Sigma_{1/2}$ states in relativistic molecules like PbF. Thus the extent to which the magnetic moment of PbF is suppressed depends on details on the electronic structure that determine $G_{||}$ and $G_{\perp}$. In this chapter we describe experimental determination of these spectroscopic parameters and discuss both comparison to theory and implications for our e-EDM measurement.

4.2 G-Factors and the Zeeman interaction

In the molecular fixed frame, the Zeeman interaction can be written as,

$$H_z = \mu_B (g\mathbf{S}' + \mathbf{L}') \cdot \mathbf{B}' = \mu_B \sum_{t=-1}^{1} (-1)^t G'^1_{-t} B'^1_t \tag{4.2}$$

where, $G'^1_{-t} = \mu_B (g S'^1 + L'^1)$.

We now assume the molecular fixed electronic wave functions for states of $\Omega = \Lambda + \Sigma$

are given by,

$$\left|\Omega_{1/2}\right\rangle = \sum_{l=1}^{\infty} c_0^l \left|l,0\right\rangle \left|1/2\right\rangle + c_1^l \left|l,1\right\rangle \left|-1/2\right\rangle \tag{4.3}$$

$$\left|\Omega_{-1/2}\right\rangle = \sum_{l=1}^{\infty} c_0^l \left|l,0\right\rangle \left|-1/2\right\rangle + c_1^l \left|l,-1\right\rangle \left|1/2\right\rangle . \tag{4.4}$$

where, $|l,m\rangle$ and $|\pm 1/2\rangle$ are suitable wave functions that describe orbital and spin degrees of freedom. Of the twelve possible matrix elements of $\left\langle \Omega^{'}|G_t^{'1}|\Omega\right\rangle$ (with $t = 0, \pm 1$ and Ω, $\Omega^{'} = \Omega_{\pm 1/2} = \pm 1/2$), only four are non zero, requiring only two nontrivial parameters,

$$G_{||} = 2\left\langle \Omega_{1/2}\right| G_0^{'1} \left|\Omega_{1/2}\right\rangle = -2\left\langle \Omega_{-1/2}\right| G_0^{'1} \left|\Omega_{-1/2}\right\rangle = \sum_{l=1}^{\infty} \left(-g(|c_1^l|^2 - |c_0^l|^2) + 2|c_1^l|^2\right) \tag{4.5}$$

$$G_{\perp} = \sqrt{2}\left\langle \Omega_{-1/2}\right| G_{-1}^{'1} \left|\Omega_{1/2}\right\rangle = -\sqrt{2}\left\langle \Omega_{1/2}\right| G_{+1}^{'1} \left|\Omega_{-1/2}\right\rangle = \sum_{l=1}^{\infty} \left(g|c_0^l|^2 + \sqrt{l(l+1)}|c_1^{l^*} c_0^l|\right) \tag{4.6}$$

According to Eq. 4.5 and Eq. 4.6 we see that for a pure π orbital $G_{||} = 2 - g, G_{\perp} = 0$. Simillarly, for a pure σ orbital $G_{||} = G_{\perp} = g$. However, neither is true for ground state of PbF because it is a mixed state of π and σ orbitals.

If we were to be able to freeze the rotational motion of the PbF molecule, Eq. 4.2 would predict the expected Zeeman interaction. However, the Zeeman interaction of a rotating molecule requires consideration of the average magnetic field as viewed from the frame of the tumbling molecule.

Ignoring hyperfine structure, we may consider a state described by $|J, M, \Omega\rangle$. In

this case, the Zeeman interaction matrix elements are given by,

$$
\begin{aligned}
(H_z)_{J',M',\Omega';J,M,\Omega} &= \mu_B \left\langle J', M', \Omega' \left| \sum_{t=-1}^{1} (-1)^t G'^1_t B'^1_t \right| J, M, \Omega \right\rangle \\
&= \mu_B \sum_{t=-1}^{1} (-1)^t \left\langle J', M', \Omega' \left| B'^1_t \right| J, M, \Omega \right\rangle \left\langle \Omega' \left| G'^1_t \right| \Omega \right\rangle \quad (4.7)
\end{aligned}
$$

At this juncture we write the magnetic field tensor in terms of its lab frame components,

$$
\begin{aligned}
(H_z)_{J',M',\Omega';J,M,\Omega} &= \mu_B \sum_{s,t=-1}^{1} (-1)^t \left\langle J', M', \Omega' \left| D^1_{st} B'^1_s \right| J, M, \Omega \right\rangle \left\langle \Omega' \left| G'^1_t \right| \Omega \right\rangle \\
&= \mu_B \sum_{s,t=-1}^{1} (-1)^t B'^1_s \left\langle J', M', \Omega' \left| D^1_{st} \right| J, M, \Omega \right\rangle \left\langle \Omega' \left| G'^1_t \right| \Omega \right\rangle \\
&= \mu_B \sum_{s,t=-1}^{1} (-1)^t B'^1_s \times \\
&\qquad \int \left(D^{J'}_{M'\Omega'} D^1_{st} D^{*J}_{M\Omega} \right) d\mathbf{\Omega} d\chi \left\langle \Omega' \left| G'^1_t \right| \Omega \right\rangle \qquad (4.8)
\end{aligned}
$$

Here we may express $\left\langle \Omega' \left| G'^1_t \right| \Omega \right\rangle$ in terms of $G_{||}$ and $G_\perp$ using Eq. 4.5 and 4.6. We also may evaluate the Wigner rotation triple integral using standard results [48]. In actuality more work must be done to both incorporate the hyperfine interaction and write the result in parity ($|\Omega|$, p_s) rather than (I, Ω) basis [8]. The result of such a complete analysis is given in Ref.[8] and below,

$$
\begin{aligned}
&\mu_B \left\langle F', J', M', p'_s \right| \sum_{t=-1}^{1} (-1)^t \mathbf{G}'^1_{-t} \mathbf{B}'^1_t \left| F, J, M, p_s \right\rangle \\
= \;& \delta_{p'_s,p_s} \delta_{I',I} \frac{(-1)^{I+J'+F'}}{4} \sqrt{(2F+1)(2F'+1)(2J+1)(2J'+1)} \left\{ \begin{array}{ccc} J' & F' & I \\ F & J & I \end{array} \right\} \times \\
& \left(\frac{1}{J_< + 1} + \frac{\delta_{J,J'}}{J} \right) \left((J' - J - \frac{\delta_{J,J'}}{2J+1}) G_{||} - p_s (-1)^{J-1/2} G_\perp \right) \times \\
& B^1_{M-M'} (-1)^{F'-M} \left(\begin{array}{ccc} F' & 1 & F \\ -M' & M'-M & M \end{array} \right) \qquad (4.9)
\end{aligned}
$$

4.3 State dependent g-factors

Hamiltonian for $^{208}Pb^{19}F$ in the absence of external fields can be written as,

$$H_{sr} = \beta \mathbf{J^2} - \Delta \mathbf{S'} \cdot \mathbf{J} + \mathbf{I} \cdot \widehat{A} \cdot \mathbf{S'} \tag{4.10}$$

For the field free situation, J states are mixed. However, F is a good quantum number. Since parity operator commutes with the Hamiltonian, given F-state only mix with other F-state with the same parity. For this reason spin rotational Hamiltonian can be described by simple 2×2 matrix.

Letting, $J = F + \frac{q}{2}$, $q = \pm 1$ we find the matrix elements,

$$\begin{aligned} \langle F, J, p_s | \, H_{sr} \, | F, J, p_s \rangle &= \left(BJ(J+1) - D(J(J+1))^2 - \frac{\Delta}{4} - \chi q \frac{\Delta}{2}(J + \frac{1}{2}) \right) \delta_{q',q} \\ &\quad - \left(\frac{\chi A_\perp}{4} + \frac{A_{||} + \chi A_\perp}{4(2F+1)} q \right) \delta_{q',q} \\ &\quad + \left((A_{||} + \chi A_\perp) \frac{\sqrt{F(F+1)}}{2F+1} \right) \delta_{q',q} \end{aligned} \tag{4.11}$$

where, $\chi = p_s(-1)^F$. More details on the derivation of spin rotational Hamiltonian can be found elsewhere [8]. We use this Hamiltonian to find field free wave functions in order to apply first order perturbation theory. Using the Zeeman interaction described in Eq. 4.9 and ignoring rotational state mixing, the g-factors can be derived as,

$$\begin{aligned} g(F, J, p_s) &= \frac{\langle F, J, I, M, p_s | \, H_{zmn} \, | F, J, I, M, p_s \rangle}{M \mu_B B} \\ &= \frac{1}{(2F+1)(2J+1)} G_{||} - 2 p_s (-1)^F \frac{F - J}{2F+1} G_\perp \end{aligned} \tag{4.12}$$

There are two corrections need to be made at 1% level for $J = 1/2$ state. The first is hyperfine mixing of J states and the second is nuclear Zeeman interaction.

4.3.1 Hyperfine mixing of J states and implication to the state dependent g-factors

We use the spin rotational Hamiltonian in Eq. 4.11 to find the amount of mixing between $J = F - 1/2$ and $J = F + 1/2$ states as a angle of mixing. The resulting mixing angle (θ) can be written as,

$$\theta(F, p_s) = \arctan\left(\frac{2\sqrt{F(F+1)}\left(A_{||} + p_s(-1)^F A_\perp\right)}{A_{||} - 2\beta(2F+1)^2 + p_s(-1)^F\left(A_\perp + (2F+1)^2\Delta\right)}\right)$$

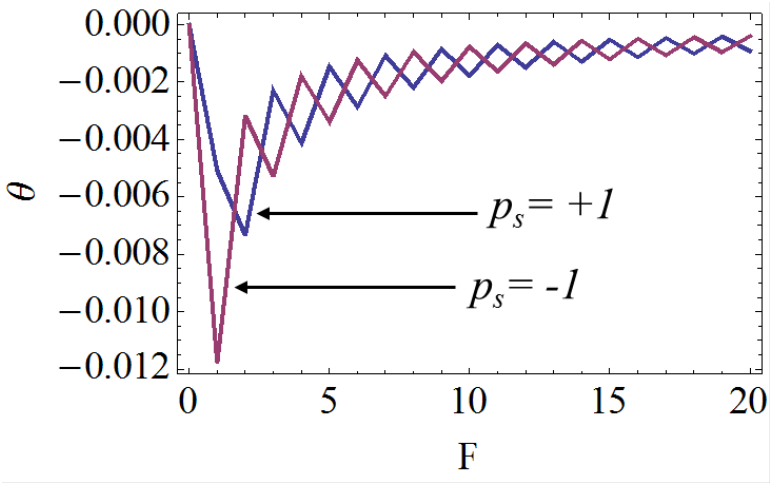

Figure 4.1: Amount of mixing of $J = F - 1/2$ and $J = F + 1/2$ rotational levels depending on hyperfine state.

We find that the effect is significant for $J = 1/2$ state in order to predict the accurate energy structure of the molecule. By taking this effect in to account we improve the state dependent g-factors shown in Eq. 4.12 as,

$$\begin{aligned} g(F, \chi, q) \;=\; & \left(\frac{\cos^2\theta}{2F+q+1} + \frac{q\sin 2\theta}{2\sqrt{F(F+1)}} + \frac{\sin^2\theta}{2F-q+1}\right)\frac{G_{||}}{2F+1} + \\ & \left(\cos^2\theta + \frac{\sin 2\theta}{2\sqrt{F(F+1)}} - \sin^2\theta\right)\frac{\chi q G_\perp}{2F+1} \end{aligned} \tag{4.13}$$

4.3.2 Nuclear Zeeman interaction and implications

The Zeeman effect due to the ^{19}F nucleus can alter the energy structure of the molecule. This perturbation is significant compared to the hyperfine mixing of different rotational levels described above. Matrix elements of this interaction can be derived as [8].

$$\begin{aligned} U_N(F,J,I) &= \mu_N g_1 \mathbf{I}\cdot\mathbf{B} \\ &= -\frac{\mu_N g_1}{\mu_B} \begin{Bmatrix} I & F & J \\ F & I & 1 \end{Bmatrix} \sqrt{I(I+1)(2I+1)} \end{aligned} \tag{4.14}$$

By taking this effect in to account in addition to mixing of J-states we find our final analytical expression for the state dependent g-factors as,

$$\begin{aligned} g(F,\chi,q) &= \left(\frac{\cos^2\theta}{2F+q+1} + \frac{q\sin 2\theta}{2\sqrt{F(F+1)}} + \frac{\sin^2\theta}{2F-q+1}\right)\frac{G_{||}}{2F+1} + \\ &\left(\cos^2\theta + \frac{\sin 2\theta}{2\sqrt{F(F+1)}} - \sin^2\theta\right)\frac{\chi q G_{\perp}}{2F+1} + \\ &\left(-\frac{\mu_N}{\mu_B}\right)\left(\frac{2(F-J)}{2J+1}\cos 2\theta + \frac{\sin^2\theta}{2F(F+1)}\right) g_1 \end{aligned} \tag{4.15}$$

4.4 Experimental Setup

The Zeeman effect of the ground state of the PbF molecule has been measured using kHz-resolution microwave spectroscopy at the University of Hanover, Germany.

PbF is produced by laser ablation (Nd:YAG, 1064 nm, 500 mJ, 20 Hz) of rotating Pb rods in the presence of diluted SF_6 contained in a noble carrier gas (Ne). PbF molecules created this way were entered to a Balle-Flygare-type [49] Fourier transform microwave (FT-MW) spectrometer at the Gottfried-Wilhelm-Leibniz-Universitt Hannover as a supersonic jet. This spectrometer uses a coaxial arrangement of the supersonic beam

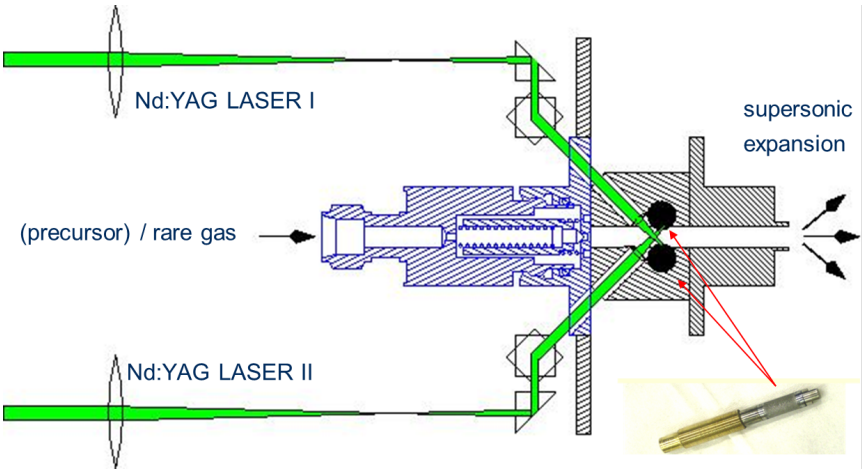

Figure 4.2: Coaxial ablation twin source of PbF (*figure is taken from Ref. [9]*)

and resonator axis ("Coaxially Oriented Beam Resonator Arrangement",COBRA) [50, 51]. The principle of operation can be briefly described as follows:

A short microwave pulse ($\sim$1 μ s) is used to excite the molecules in the cavity, as a result molecules will be polarized and the subsequent free induction decay (FID) of the oscillating macroscopic dipole moment is recorded in the time domain. Fourier transformation of this signal can be used to produce frequency domain spectrum. When COBRA configuration is used, signal doublets are observed by the Doppler effect of the supersonic jet expanding coaxially to the propagation axis of the standing wave field of the Fabry-perot-type resonator. The mean value of these frequency doublets can be used to determine resonance frequency of the rotational transition.

4.5 Analysis and Results

In order to predict Zeeman splittings of each state require the value of g_1 and the body fixed g-factors $G_{||}$ and $G_{\perp}$. The value of g_1 is taken from the literature [52]. Instead

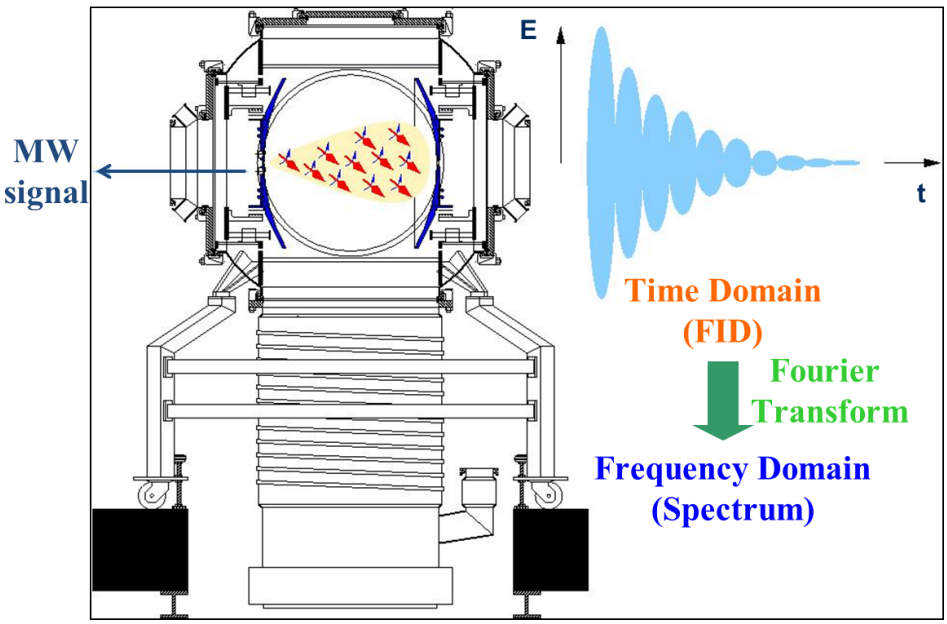

Figure 4.3: Fourier transform micro-wave spectrometer: The principle of operation (*figure is taken and modified from Ref. [9]*)

of fitting data to $G_{||}$ and $G_{\perp}$ we minimize the uncertainty due to the calibration of magnetic field by measuring the ratio $\frac{G_{||}}{G_{\perp}}$. Then we fit measured Zeeman shifts to a single variable $G_{\perp}$. Finally we combine $\frac{G_{||}}{G_{\perp}}$ and $G_{\perp}$ to determine $G_{||}$. To best determine the ratio $\frac{G_{||}}{G_{\perp}}$ we apply a magnetic field perpendicular to the microwave polarization by using Helmholtz coils. Observed Zeeman splittings of $F = 0 \leftrightarrow F = 1$ transitions are used to gain the sensitivity $\frac{G_{||}}{G_{\perp}}$ by evaluating the ratio Γ_{AB}. These splittings are shown in Fig. 4.4.

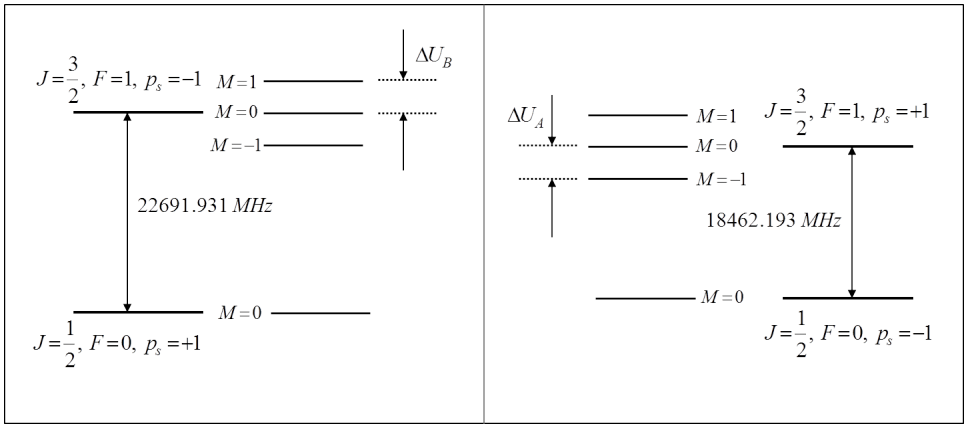

Figure 4.4: Observed Zeeman splittings for $F = 0 \leftrightarrow F = 1$ transitions (not to the scale)

$$\begin{aligned}
\Gamma_{AB} &= 4\frac{\Delta U_B + \Delta U_A}{\Delta U_B - \Delta U_A} \\
&= 4\frac{|\Delta U_B| - |\Delta U_A|}{|\Delta U_B| + |\Delta U_A|} \; for\, |\Gamma_{AB}| < 4 \\
&\approx 0.0046 + 1.009\frac{G_{||}}{G_\perp} + 2.991\frac{\mu_N}{\mu_B}\frac{g_1}{G_\perp} \\
&= -0.371 \pm 0.005
\end{aligned} \tag{4.16}$$

In the expression of Γ_{AB}, absolute values of splittings are necessary because this experiment is only sensitive to magnitude but not to the sign of energy differences.

We can approximate the contribution from the Zeeman effect due to ^{19}F nucleus, $2.991\frac{\mu_N}{\mu_B}\frac{g_1}{G_\perp} \approx 0.026$ by assuming CRC handbook value [52] for $g_1 = 5.25773$ and $G_\perp = -0.326$ [53]. From this approximation, we see that nuclear Zeeman effect is roughly a factor of 5 bigger correction to the Zeeman interaction than the effect of hyperfine mixing of different rotational levels.

Our determination of $G_\perp$ is limited by magnetic field calibration. In order to test magnetic field calibration we experimentally determine $G_\perp$ by applying parallel

($\Delta M = 0$) transitions and perpendicular ($|\Delta M| = 1$) transitions separately. Results are given below.

$$G_\perp = -0.39 \pm 0.01 \ (\Delta M = 0 \ Transitions)$$

$$G_\perp = -0.38 \pm 0.01 \ (|\Delta M| = 1 \ Transitions)$$

These results indicate that our magnetic field calibration error is roughly the statistical error of our measurement. Our final results for $G_\perp$ and $G_{||}$ are given in table 4.1 with a comparison of few existing theoretical models.

Table 4.1: Results with a comparison of theory

	this work (66% confidence)	ref. [53]	ref. [54]	ref. [55]
$G_\perp$	-0.38 ± 0.02	$-0.438 < G_\perp < -0.269$	-0.326	-0.319
$G_{||}$	0.12 ± 0.01	$0.034 < G_{||} < 0.114$	0.04	0.082

Throughout the data analysis we assumed that $G_\perp < 0$. If we assumed $G_\perp > 0$, the variance of the fit is approximately 3 times bigger than the variance of the fit assuming $G_\perp < 0$. This indicates that even though the experiment is insensitive to orientation of the molecules, our data are sensitive to the sign of $G_\perp$ through the contribution of Zeeman effect due to ^{19}F nucleus. Therefore the result presented here support the theoretical prediction [53] that $G_\perp < 0$.

By using these measurements and g_1, we find the g-factor of the state that we are interested in PbF molecule as ≈ 0.04. This small g-factor will be a great advantage in order to gain sensitivity to the e-EDM by controlling over the effect from background magnetic fields.

Chapter 5

Investigation of optical sources of metastable Krypton

5.1 Introduction

Isotopic detection of metastable Kr (specially, ^{81}Kr and ^{85}Kr) has major practical applications in archaeological dating and nuclear activity monitoring all around the world.

Table 5.1: Isotopic abundance of Kr in atmosphere [7]

Isotope	**Atmospheric abundance**	**Half-life**	**Source**
^{81}Kr	1×10^{-12}	229,000 yr	Cosmic-ray induced reaction
^{85}Kr	2×10^{-11}	10.8 yr	Nuclear fuel reprocessing

However, detecting extremely small natural abundance specially ^{81}Kr in water samples would be challenging and limits the use of this tracer in real world applications. In this regard, the technique, atom trap trace analysis (ATTA) developed by Z. T. Lu and co-workers has demonstrated a remarkable success among all other atom counting method such as low level counting (LLC) and accelerator mass spectrometry (AMS) [10]. The heart of the ATTA instrument is a magneto optical trap (MOT). However, according to today's technology trapping of ground state Kr atoms are impossible due to limited access of vacuum ultraviolet (VUV) lasers at 124 nm. Instead, it can be trapped via $5s[3/2]_2$ metastable state (Kr*) which provides ground state like environment with higher internal energy and longer lifetime ($\approx 40s$) in a magneto

optical trap. Therefore, in order to detect Kr, metastable Kr needs to be created efficiently. Currently, the production of metastable Kr is realized by electron impact excitation using RF-driven discharge. The excitation efficiency achieved by this method is only about 10^{-3} (the ratio between Kr* atom flux and the ground state atom flux in the forward direction) [56]. This limits the Kr isotope detection efficiency to isotopic abundance one part in 10^{12} level in the current ATTA setup. The schematic layout of the experimental setup is shown in Fig. 5.1.

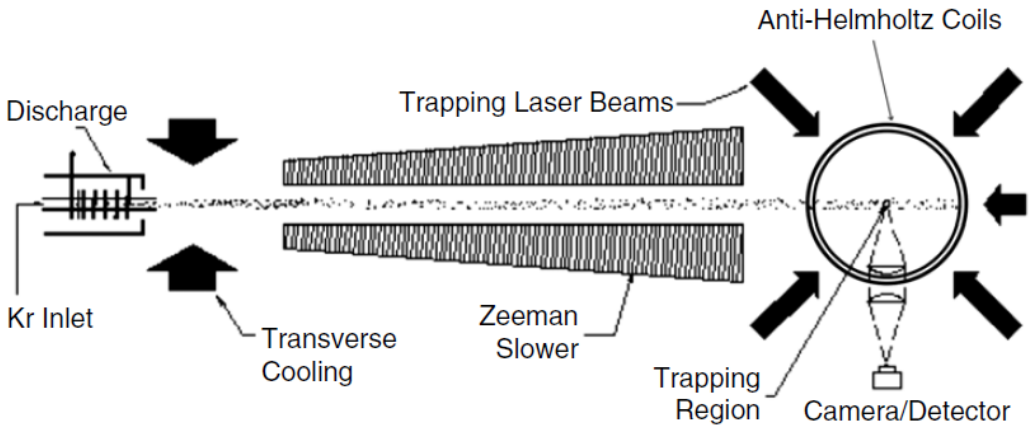

Figure 5.1: Experiment setup of the ATTA for Kr isotope detection. Metastable Kr atoms are produced in RF-discharge. Atomic beam is transversely cooled by counter propagating laser beams and slowed down by Zeeman slower. Fluorescence of individually trapped atoms is detected (*Figure is taken from Ref.[10]*)

In the magneto optical trap Kr isotopes are captured and detected via laser induced fluorescence (LIF). At a time, only a selective isotope can be trapped by red-detuning the laser frequency within few natural line widths of the interested transition. Other isotopes are off-resonance to this laser frequency and can not be

trapped. ATTA instrument is capable of capturing even a single atom selectively thus avoiding contamination of the signal by other isotopes, atoms or molecules presence in the sample. This can be considered as an unique feature with compared to other atom counting methods that exist today.

Besides the method RF-discharge, a production of metastable Kr atoms by optical excitation has also been tested. In this method, ground state atoms are excited to $5p[3/2]_2$ using two photon excitation (see Fig. 5.2). Then the metastable Kr is created via the spontaneous emission of $5p[3/2]_2$ level to $5s[3/2]_2$. The 124 nm photon required in first step has been created using Kr-discharge lamp.

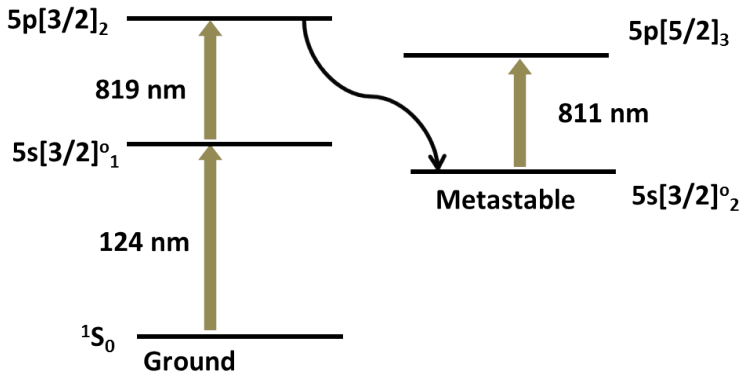

Figure 5.2: Kr atomic energy levels. Metastable atoms are produced by $1+1$ photon excitation (124 nm and 819 nm) of $5p(3/2)_2$ state and followed by a spontaneous decay. 811 nm laser is used as cycling transition in the trap

Even though in this method a less excitation efficiency is achieved it outlines some advantages over the discharge method. Some of the problems with the discharge method are sample loss by hitting walls and it requires minimum milli-torr pressure

to operate. These problems can be overcome by the optical excitation source.

The major limitation of this method which prevents competing with the RF-driven discharge is lack of a sufficiently intense 124 nm photon source. 124 nm laser sources may push ATTA detection of rare isotopes of Kr to a remarkable level.

5.2 Applications of Kr-ATTA

5.2.1 Radioactive dating

Because of its much longer half life the cosmogenic ^{81}Kr can be used for dating water and ice in the age range of $10^5 - 10^6$ years where the radiocarbon dating (half life = 5370 yr) is not applicable. As a real world application ^{81}Kr dating has been done in old ground water samples in the Nubian Aquifer located underneath eastern end of Sahara Desert [10]. However, each measurement required more than 1000 liters due to low trap loading efficiency of ATTA indicated that further improvements needed for routine scientific applications. As a result of this study age of the water as well as hydrologic behavior (flow patterns and speeds) of the aquifer is determined. These results can be useful in climate history and water resource management in the region.

Ground water can be considered as the major carrier of radioisotopes from nuclear waist repositories to the surrounding environments. Therefore, by studying longterm ground water flow pattern could provide an important information about potential nuclear waist repositories.

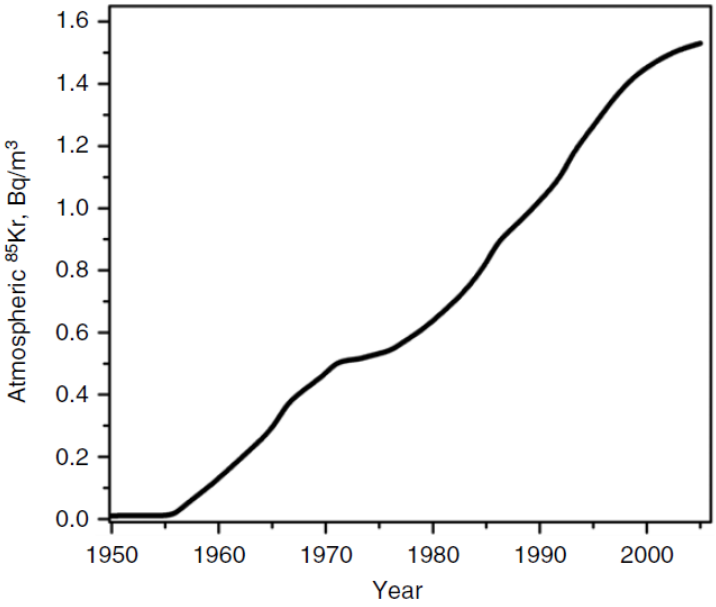

Figure 5.3: Increasing trend of annual mean values of atmospheric ^{85}kr in northern hemisphere from 1950 to 2005 [11, 12, 13] (*Figure is taken from Ref.[10]*)

5.2.2 Nuclear monitoring

^{85}Kr is produced by Uranium and Plutonium fission in nuclear reactors. It is released to the atmosphere due to an essential plutonium recovery process which is called nuclear fuel reprocessing. Therefore, monitoring air in surrounding atmosphere some hidden nuclear activities can be detected.

In addition to that ^{85}Kr can be used as as a leak detector. Monitoring in air and ground water can provide information about possible nuclear reactor leakage in the region and advanced warnings can be issued.

5.3 Experimental

As a warm up experiment we detected Krypton using 2+1 REMPI via the $5p[3/2]_2$ state. Here, neutral krypton is excited using 214 nm laser radiation. The laser radiation was produced by tripling of the output (75 mJ, 640 nm) of a Nd:YAG pumped (10 Hz, 10 ns) dye laser. Ionization signal is shown in Fig. 5.4

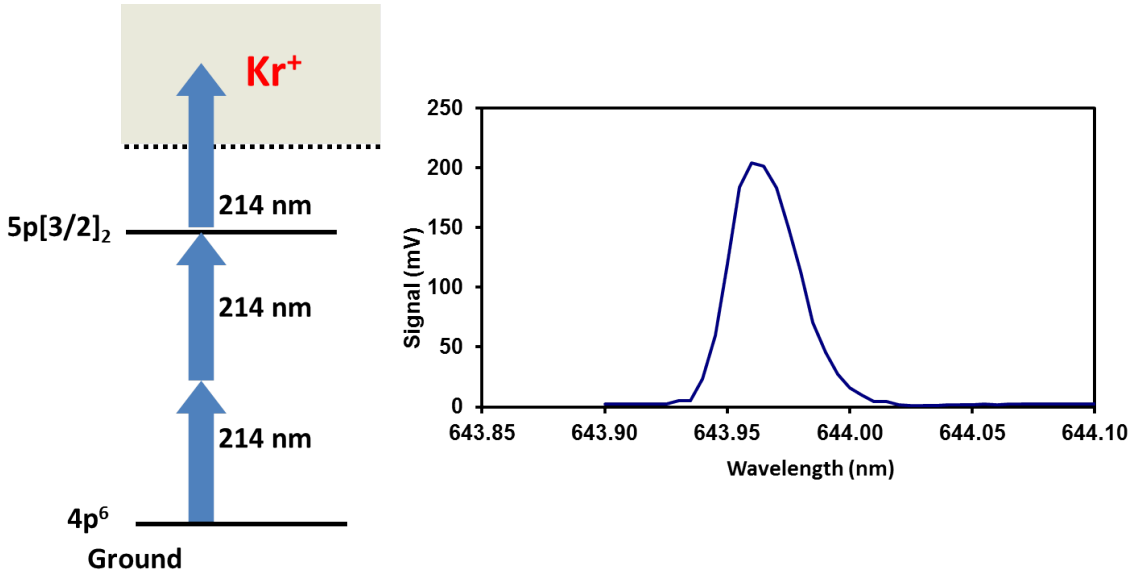

Figure 5.4: 2+1 REMPI ionization scheme and the resulting Kr ion signal

5.3.1 Attempt I

Our first attempt was to lower the 214 nm laser intensity used in the 2+1 REMPI scheme and then probe to see if any of the excited $5s[3/2]_2^0$ state was produced by spontaneous emission from the $5p[3/2]_2$ state.

214 nm laser light is focused in a capillary such a way that Kr atoms pass through the capillary are excited to $5s[3/2]_2^0$ metastable state (see Fig. 5.5. Since lifetime of

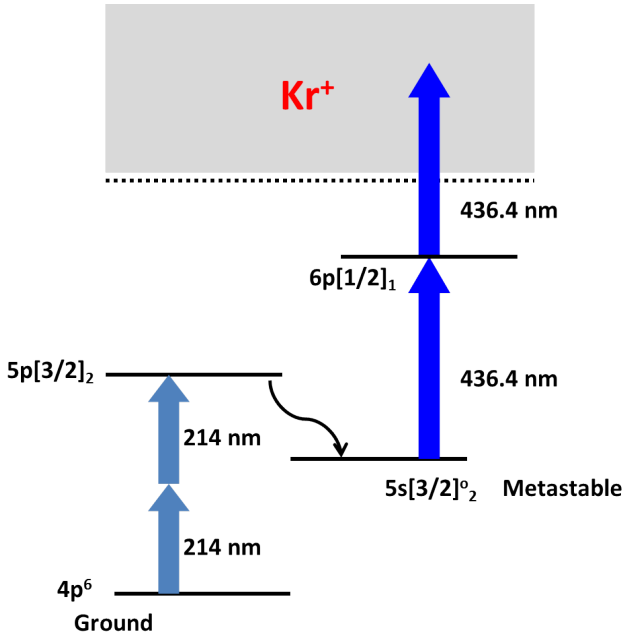

Figure 5.5: Ionization scheme for attempt I

this state is so long (40s), metastable atoms were expected to survive until they pass through the center of the detector where the ionization laser is focused. This way almost all ions were expected to detect via the $5s[3/2]^0_2$ metastable state. Our probe for metastable $5s[3/2]^0_2$ state Kr was a 1+1 probe via the $6p[1/2]_1$ state. The laser radiation for this probe was pseudo-continuous (76 MHz, 6 ps) laser radiation at 436.4 nm. An electron ion coincident detector was then used to probe for ionization events.However, we were unable to observe any successful Kr ion signal in this experiment. The possible reasons for this could be,

1. Metastable Kr atoms produced in the capillary were destroyed them self by hitting the walls.

2. Our metastable Kr production inside the capillary was very inefficient. Even

though, we lowered the 214 nm laser intensity almost all Kr ions were ionized in the capillary because of the focus of the light.

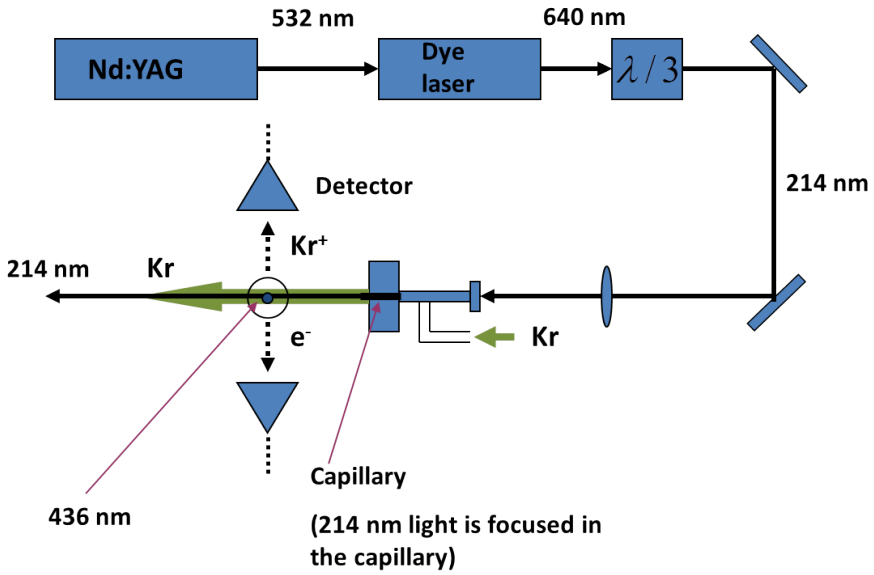

Figure 5.6: Experimental setup. 214 nm light is produced by frequency tripling of dye laser output at 640 nm. This light is focused inside a capillary tube ($\approx$ 5 mm long) such a way that Kr atoms pass through the capillary are interacted with 214 nm laser

5.3.2 Attempt II

The next idea was to populate metastable level by detuning the 214 nm laser radiation and adding a source of 760 nm (using another dye laser pumped by the same Nd:YAG laser) light in order to create near-resonant enhanced multi-photon excitation to the $5s[3/2]_2^0$ state. Unfortunately, this experiment was disrupted by a demon in our circa 1970 Nd:YAG laser. If we were able to do this experiment without any interruption, we strongly believe that we may be able to come up with some positive result because

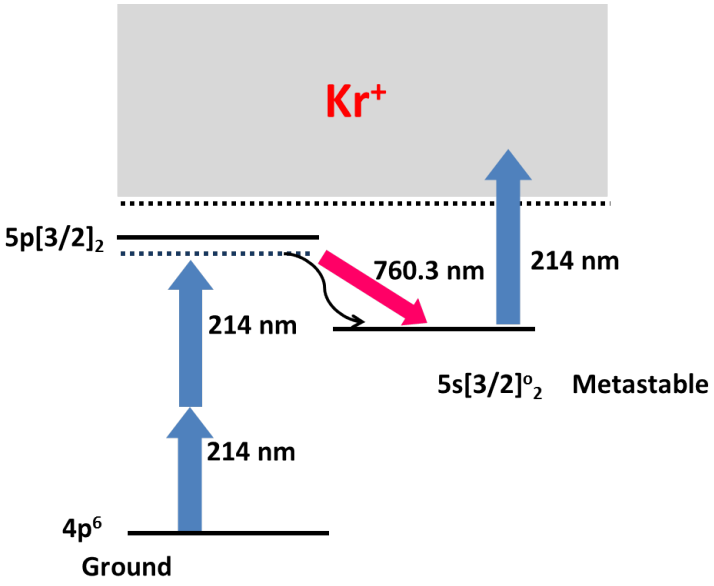

Figure 5.7: Ionization scheme for attempt II

population transfer process from near resonance $5p[3/2]_2$ state to $5s[3/2]^0_2$ state is more favorable through the 760 nm laser [57].

5.4 Results and conclusion

A laser based production of metastable Kr was attempted. In this attempt there was not exciting results to report. Couple of possible reasons which prevent this experiment a success were explained in the text. As a result, another experiment was designed and setup to create metastable Kr. However, this second attempt was interrupted by a failure of the Nd:YAG pump laser.

Chapter 6

Summary and conclusion

In 1950, Purcell and Ramsey proposed that the electron might have an electric dipole moment (e-EDM) proportional to spin. This proposal initiated a search for an e-EDM that is still ongoing. The current limit of the e-EDM ($1.05\times10^{-27}e\cdot$cm) has been placed very recently in 2011 by measuring the energy difference between $M = 1$ and $M = -1$ states of $F = 1$ hyperfine level in the ground state of YbF molecule. Today many groups (including us) are working hard to either push this limit further or measure the value of e-EDM. If found, it could point a way to new physics beyond the Standard Model as it violates CP by many orders of magnitude than it determined by today's most successful theory in particle physics. As the major part of this thesis, some work has been done towards measuring e-EDM using PbF molecules was described. Specifically we have achieved following:

- We showed that the geometric phase effect limits the viability of a cold molecular trap technique that can be employed for PbF molecules as an e-EDM probe until the technology is available to cool down molecules to ultra cold temperatures.

- The state dependent g-fators of the PbF molecule have been measured as it plays an important role in a possible e-EDM measurement.

- A precise high voltage control and switching system has been built. This device can be used to create highly uniform electric field that can be reversed in a

precise and consistent manner which is required by an e-EDM experiment based on Ramsey interferometer technique.

In order to detect Kr isotopes better than 1 part in 10^{12}, a novel rare isotope detection technique ATTA (Atom Trap Trace Analysis) developed by Z. T. Lu and co-workers require higher efficiency in the production of metastable Kr than the efficiency of current RF discharge method. In order to address this difficulty, an attempt at optical production of metastable Kr was described as the other part of this thesis. However, this experiment was disrupted by a demon in our circa 1970 Nd:YAG laser.

References

[1] E. R. Meyer and J. L. Bohn, Phys. Rev. A **78**, 010502 (2008).

[2] D. DeMille, F. Bay, S. Bickman, D. Kawall, D. Krause, S. E. Maxwell, and L. R. Hunter, Phys. Rev. A **61**, 052507 (2000).

[3] . Preprint, Learnhardt.

[4] A. N. Petrov, 66th International Symposium on Molecular Spectroscopy.

[5] www-personal.umich.edu/ aehardt/research/WC.html.

[6] J. J. Hudson, B. E. Sauer, M. R. Tarbutt, and E. A. Hinds, Phys. Rev. Lett. **89**, 023003 (2002).

[7] R. Firestone and V. E. Shirley, *Table of Isotopes* (John Wiley, New York, 1996).

[8] R. Mawhorter and et al., Phys. Rev. A **00**, (2011).

[9] J. U. Grabow, Private communication .

[10] Z.-T. Lu and P. Mueller, Advances in Atomic, Molecular, and Optical Physics **58**, 173 (2010).

[11] W. Weiss, H. Sartorius, H. Stockurger, and T. E. Florkowski, IAEA Vienna 29 (1992).

[12] L. Wilhelmova, M. Tomasek, and K. Stukheil, Bio. Trace Element Res. **43**, 725730 (1992).

[13] Bundesamt fuer Strahlenschutz, The Federal Office for Radiation Protection, Jahresbericht (Annual Report) (2007).

[14] E. Purcell and N. Ramsey, Phys. Rev. **78**, 807 (1950).

[15] J. Schwinger, Phys. Rev. **91**, 493496 (1953).

[16] B. C. Regan, E. D. Commins, C. J. Schmidt, and D. DeMille, Phy. rev. **88**, 4 (2002).

[17] P. Sandars, Atomic Physics **14**, 71 (1975).

[18] J. J. Hudson, D. M. Kara, I. J. Smallman, B. E. Sauer, M. R. Tarbutt, and E. A. Hinds, Nature **473**, 493496 (2011).

[19] A. E. Leanhardt, J. L. Bohn, H. Loh, P. Maletinsky, E. R. Meyer, L. C. Sinclair, R. P. Stutz, and E. A. Cornell, arXiv.org (2011).

[20] J. L. ad E.R. Meyer, R. Paudel, J. Bohn, and A. Leanhardt, Journal of Modern Optics **56**, 20052012 (2009).

[21] A. C. Vutha, W. C. Campbell, Y. V. Gurevich, N. R. Hutzler, M. Parsons, D. Patterson, E. Petrik, B. Spaun, J. M. Doyle, G. Gabrielse, and D. DeMille, J. Phys. B **43**, (2010).

[22] D. DeMille, F. Bay, S. Bickman, D. Kawall, D. Krause, S. E. Maxwell, and L. R. Hunter, Phys. Rev. A **61**, 052507 (2000).

[23] N. E. Shafer-Ray, Phys. Rev. A **73**, 034102 (2006).

[24] P. Sivakumar, Ph.D. thesis, University of Oklahoma, USA, 2009.

[25] C. P. McRaven, P. Sivakumar, and N. E. Shafer-Ray, Phys. Rev. A **75**, (2007).

[26] P. Sivakumar, C. P. McRaven, D. Combs, and N. E. Shafer-Ray, Phys. Rev. A **77**, (2008).

[27] C. P. McRaven, P. Sivakumar, and N. E. Shafer-Ray, Phys. Rev. A **78**, (2008).

[28] P. Sivakumar, C. McRaven, P. Rupasinghe, T. Yang, N. Shafer-Ray, T. J. Sears, and G. E. Hall, Mol. Phys. 1 (2010).

[29] L. D. Alphei, J.-U. Grabow, A. N. Petrov, R. Mawhorter, B. Murphy, A. Baum, T. J. Sears, T. Z. Yang, P. M. Rupasinghe, C. P. McRaven, and N. E. Shafer-Ray, Phys. Rev. A **83**, 040501 (2011).

[30] E. Purcell and N. Ramsey, Phys Rev **78**, 807 (1950).

[31] N. Fortson, P. Sandars, and S. Barr, Physics Today 33 (2003).

[32] E. D. Commins, S. B. Ross, D. DeMille, and B. Regan, Physical Review A **50**, 2960 (1994).

[33] B. Regan, E. D. Commins, C. J. Schmidt, and D. DeMille, Physical Review Letters **88**, 71805 (2002).

[34] D. Egorov, J. Weinstein, D. Patterson, B. Friedrich, and J. M. Doyle, Physical Review A **63**, 30501 (2001).

[35] M. R. Tarbutt, H. L. Bethlem, J. J. Hudson, V. L. Ryabov, V. A. Ryzhov, B. E. Sauer, G. Meijer, and E. A. Hinds, Physical review letters **92**, 173002 (2004).

[36] D. DeMille, F. Bay, S. Bickman, D. Kawal, J. D. Krause, S. Maxwell, and L. Hunter, Physical Review A **61**, 52507 (2000).

[37] J. Hudson, B. Sauer, M. Tarbutt, and E. Hinds, Physical Review Letters **89**, 23003 (2002).

[38] T. Kohler, K. Goral, and P. S. Julienne, Reviews of modern physics **78**, 1311 (2006).

[39] J. J. Gilijamse, J. Kupper, S. Hoekstra, N. Vanhaecke, S. Y. T. v. d. Meerakker, and G. Meijer, Physical Review A **73**, 63410 (2006).

[40] J. Ye, S. Blatt, M. M. Boyd, S. M. Foreman, E. R. Hudson, T. Ido, B. Lev, A. D. Ludlow, B. C. Sawyer, and B. Stuhl, AIP conference proceedings **869**, 80 (2007).

[41] B. E. Sauer, H. T. Ashworth, J. J. Hudson, M. R. Tarbutt, and E. A. Hinds, AIP conference proceedings **869**, 44 (2007).

[42] *Some Recent Developments in the Theory of Molecular Energy Levels*, *Advances in Spectroscopy II*, edited by Longuet-Higgens (Interscience Publishers, New York, 1961).

[43] M. Rupasinghe and N. E. Shafer-Ray, Phy. rev. **78**, 10 (2008).

[44] N. E. Shafer-Ray, A. J. Orr-Ewing, and R. N. Zare, Journal of Physical Chemistry **95**, 7591 (1995).

[45] N. Shafer-Ray, K. A. Milton, B. R. Furneaux, E. Abraham, and G. R. Kalbfleisch, Physical Review A **67**, 45401 (2003).

[46] S. A. Meek, E. R. I. Abraham, and N. E. Shafer-Ray, Physical Review A **71**, 65402 (2005).

[47] M. Kozlov, V. Fomichev, Y. Y. Dmitriev, L. Labzovsky, and A. Titov, J. Phys. B: At. Mol. Opt. Phys. **20**, 4939 (1987).

[48] R. Zare, *Understanding Spatial Aspects in Chemistry and Physics* (Wiley Interscience, New York, 1988).

[49] T. J. Balle and W. H. Flygare, Rev. Sci. Instrum. **52**, 33 (1981).

[50] W. S. J.-U. Grabow and Z. Naturforsch., A: Phys. Sci. **45A**, 1043 (1990).

[51] J.-U. Grabow, W. Stahl, and H. Dreizler, Rev. Sci. Instrum. **67**, 4072 (1996).

[52] *CRC Handbook of Chemistry and Physics, 90th ed.* (CRC Press, Boca Raton, FL, 2008).

[53] M. Kozlov, V. Fomichev, Y. Y. Dmitriev, L. Labzovsky, and A. Titov, J. Phys. B **20**, 4939 (1987).

[54] Y. Y. Dmitriev, Y. G. Khait, M. Kozlov, L. Labzovsky, A. Mitrushenkov, A. Shtoff, and A. Titov, Phys. Lett. A **167**, 280 (1992).

[55] K. I. Baklanov, A. N. Petrov, A. V. Titov, and M. G. Kozlov, Phys. Rev. A **82**, (2010).

[56] C. Chen, K. Bailey, Y. Li, T. O'Connor, and L. Z.-T., Review of scientific instruments **72**, (2001).

[57] C. McRaven, J. Alnis, B. Furneaux, and N. Shafer-Ray, J. Phys. Chem. A **107**, 7138 (2003).

Appendix A

Schematic layout of the high voltage control and switching system as two separate units

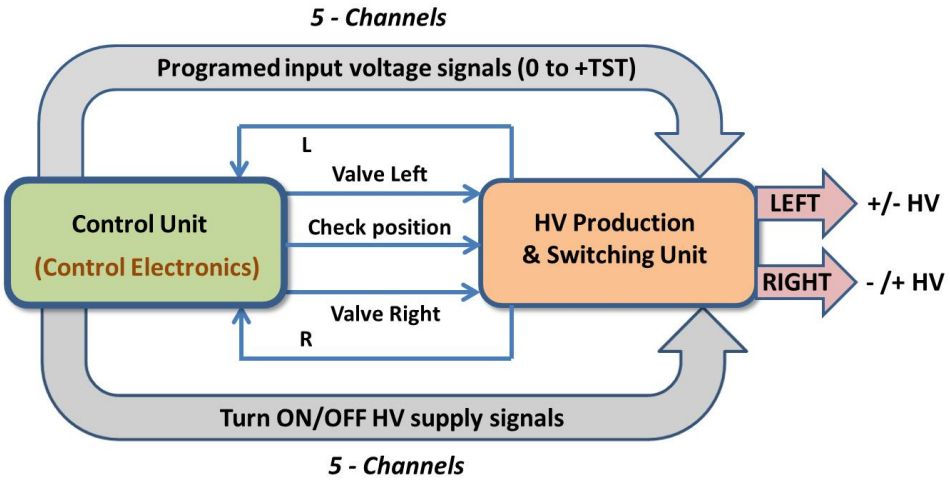

Figure A.1: Schematic view of the high voltage switching control system. The control unit mostly contains digital electronics and supply low voltage (0-5 V) control signals to the HV production and switching unit. HV production and switching unit contains high voltage power supplies and pneumatic controls for switching

Detailed description of the design of digital control unit, HV production and switching unit, and computer remote control of the device can be found in Appendices B, C, and D respectively.

Appendix B

High voltage control unit

This device mostly contains digital electronics and supply programed voltages (0 to +TST(in this case +5V) or 0 to -TST(in this case -5V)) as well as switching control signals to the high voltage production and switching unit. This unit consists of one switching control circuit board (Master board) and five identical high voltage control circuit boards (Channels). State diagrams of these circuits are shown in Fig.B.1 and Fig.B.2. Each channel can be used to increase or decrease voltage gradually until it reaches a desired voltage. By using computer interface this voltage can be achieved by several steps such a way that each step reaches some voltage below the desired value gradually from zero and then gradually decreases to zero. This procedure continues several times until the final voltage is achieved. When high voltage production and switching unit is connected, this will help to clean up the plates so that unnecessary sparks can be avoided. Description about these channels can be found in Table B.1.

B.1 The Front panel

As shown in Fig.3.2 the front panel consists of five identical sub panels for five different channels. Binary coded decimal (BCD) input can be used to input the magnitude of high voltage that need to be produced. The main function of each channel is to track the input voltage. Table B.2 summarizes the different input switches and outputs in the front panel of each individual channel. In addition to that there are two pushbutton

Table B.1: Description of high voltage channels

Channel name	**Description**
HIGH VOLTAGE	High voltage supply for the electric field in the drift region
POLARIZATION	High voltage supply for the electric field in order to polarize the molecules
EXTRACTION	High voltage supply for the electric field in extraction region
+MCP	Positive high voltages needed for the microchannel plates in the detector (this voltage is divided in to 4-different voltages in a separate unit)
-MCP	Negative high voltages needed for the microchannel plates in the detector (this voltage is divided in to 4-different voltages in a separate unit)

switches REQST LEFT and REQST RIGHT which control the switching of all the high voltages produced by all channels. The action of these switches are shown in Fig.C.1. When a channel is turned ON, following three things can be happened.

1. It turns on corresponding high voltage power supplies (DC/DC comparators) in the high voltage production and switching unit.

2. If TRCK/ZERO switch is in TRCK position it increases the voltage gradually until the input voltage is achieved (Tracking). This is done by sending programed input to the corresponding high voltage power supply in the high voltage production and switching unit.

3. If TRCK/ZERO switch is in ZERO position it does nothing. Output voltage

remains zero.

When a channel is turned OFF following three things can be happened.

1. If TRCK/ZERO switch is in TRCK position it decreases the voltage gradually until zero and then shuts down itself. This is done by sending programed input to the corresponding high voltage power supply in the high voltage production and switching unit.

2. If TRCK/ZERO switch is in ZERO position it shuts down itself immediately. In this position it is safe do so because output voltage is zero.

3. It turns off corresponding high voltage power supplies (DC/DC comparators) in the high voltage production and switching unit when it shuts down itself.

B.2 Control inputs, outputs and State diagrams

Fig.B.1 and Fig.B.2 shows the state diagrams that describe the design of high voltage On/Off electronics and switching electronics respectively. Control inputs and outputs can be found in Table B.3 and Table B.4. All the schematics related to this unit can be found in Appendix A and B.

B.3 Schematics

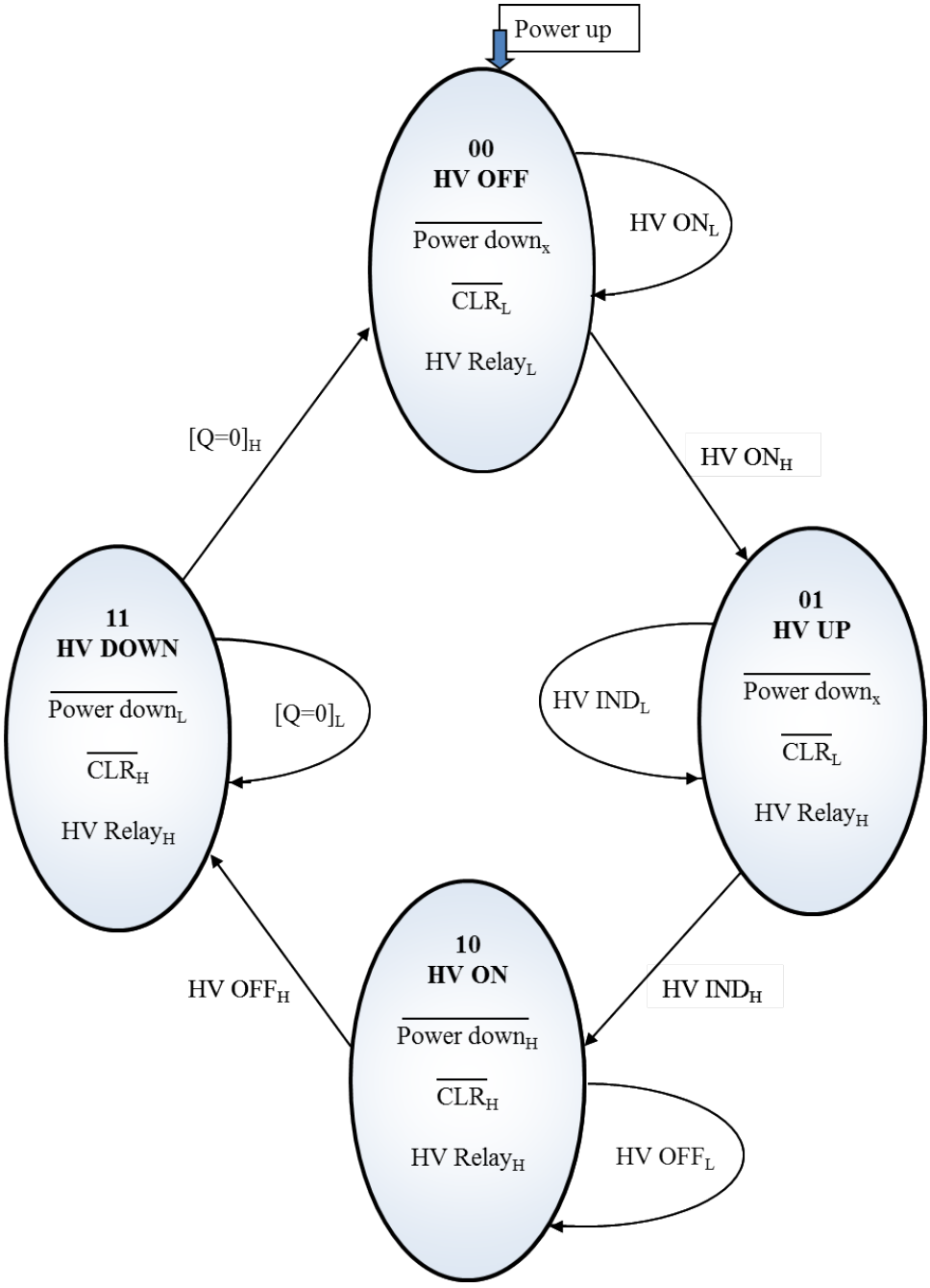

Figure B.1: State diagram of high voltage control unit electronics for each channel

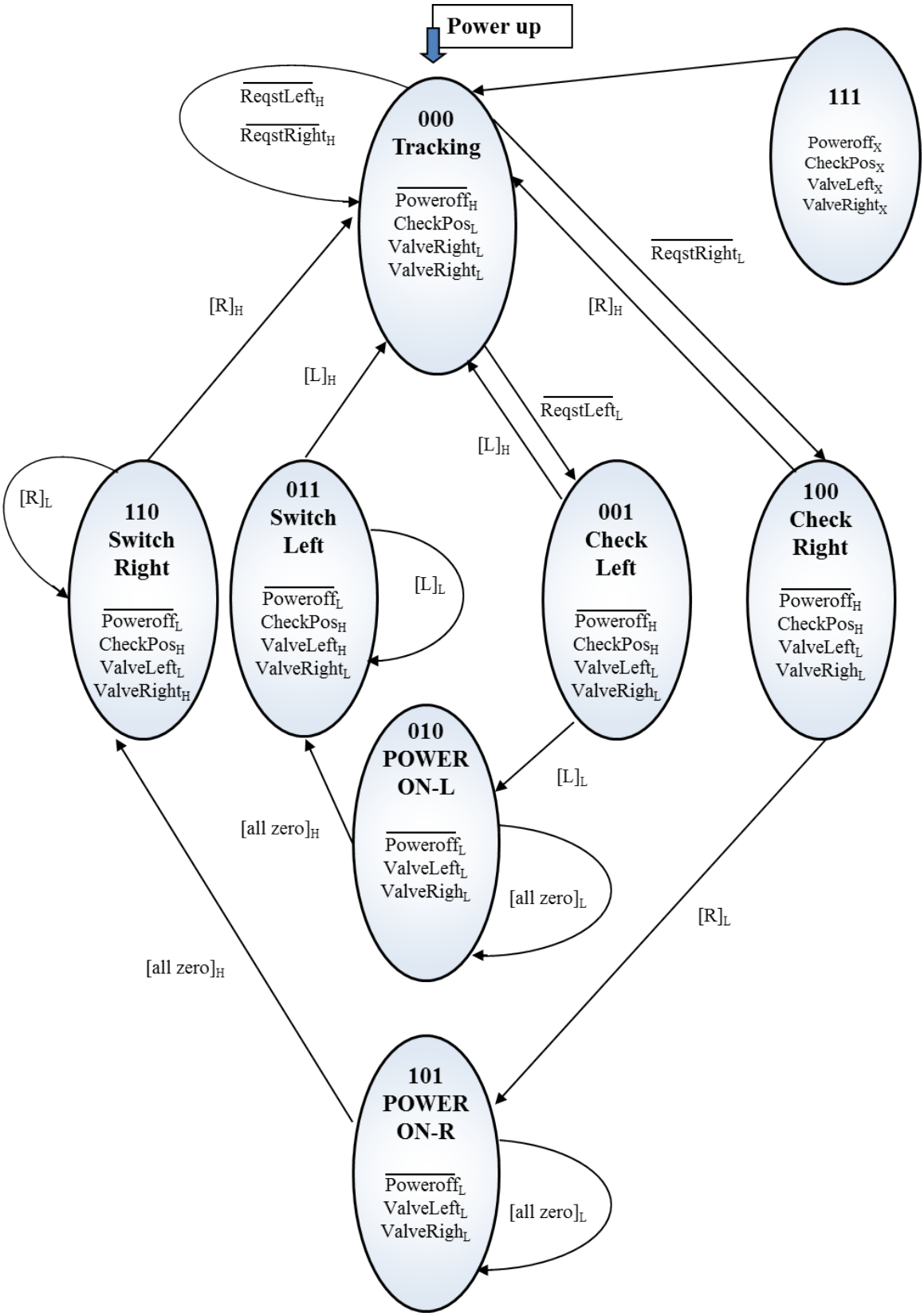

Figure B.2: State diagram of high voltage switching electronics for all channels.

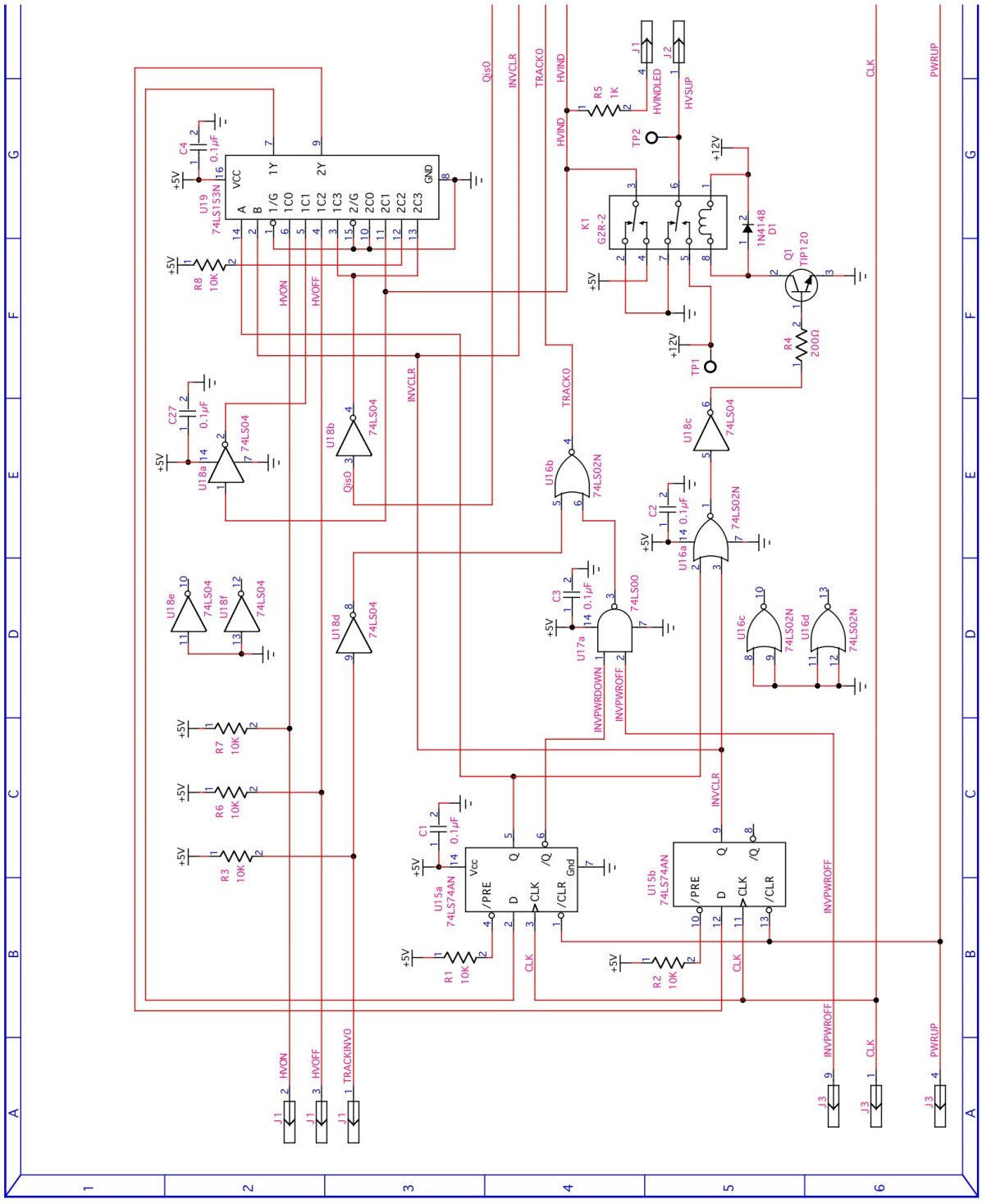

Figure B.3: Schematic of high voltage control unit electronics for each channel (part 1 of 4)

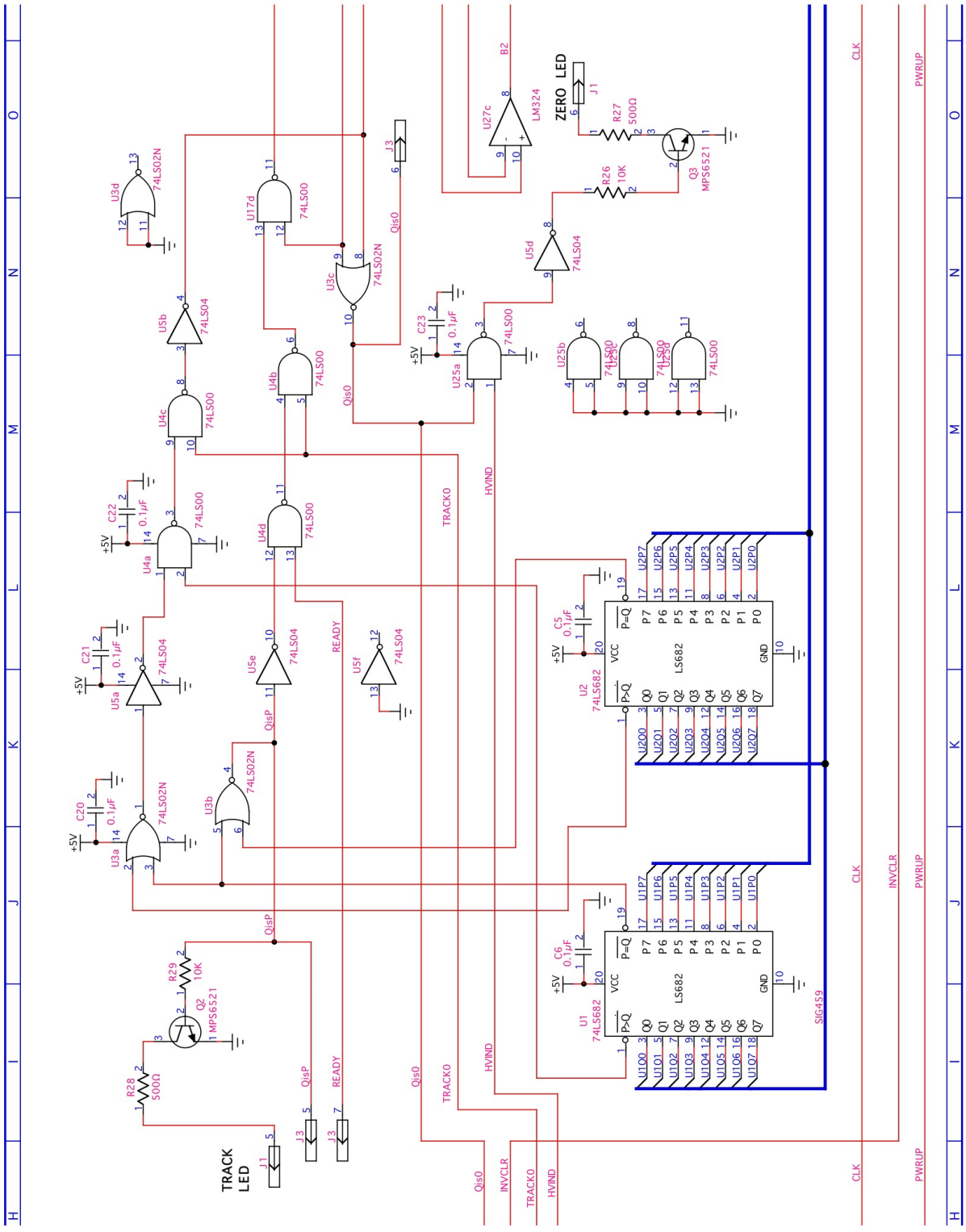

Figure B.4: Schematic of high voltage control unit electronics for each channel (part 2 of 4)

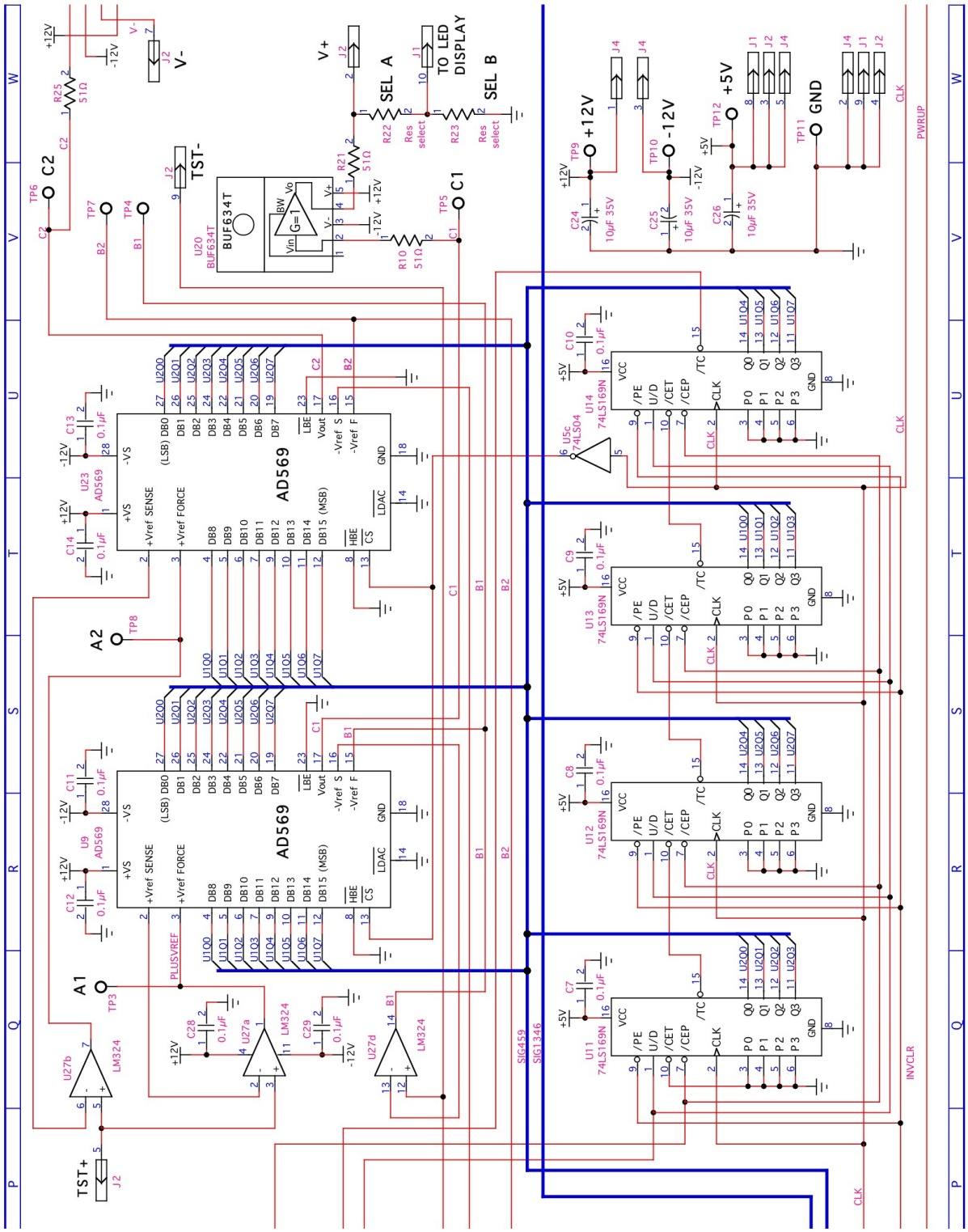

Figure B.5: Schematic of high voltage control unit electronics for each channel (part 3 of 4)

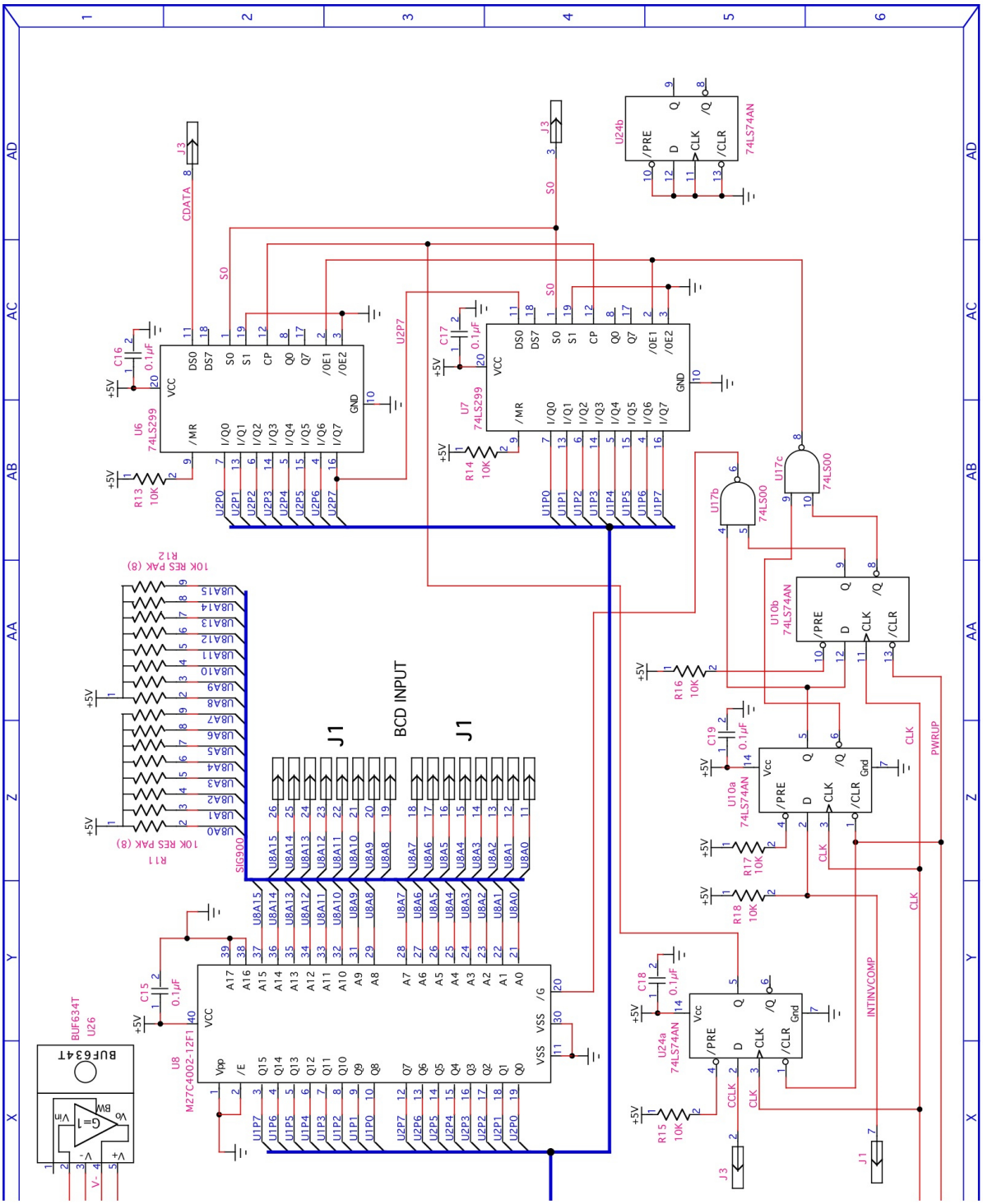

Figure B.6: Schematic of high voltage control unit electronics for each channel (part 4 of 4)

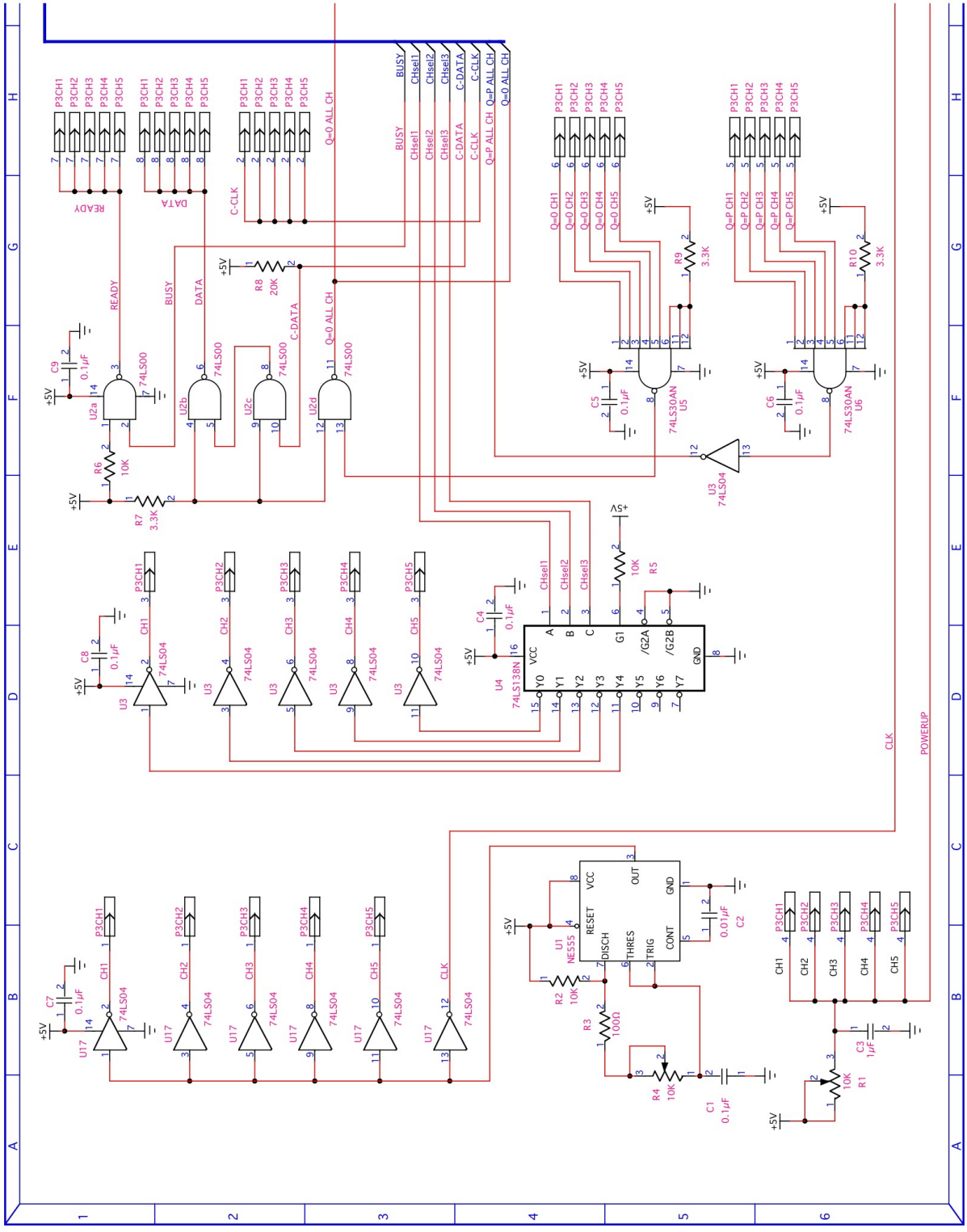

Figure B.7: Schematic of high voltage switching electronics for all channels (part 1 of 3)

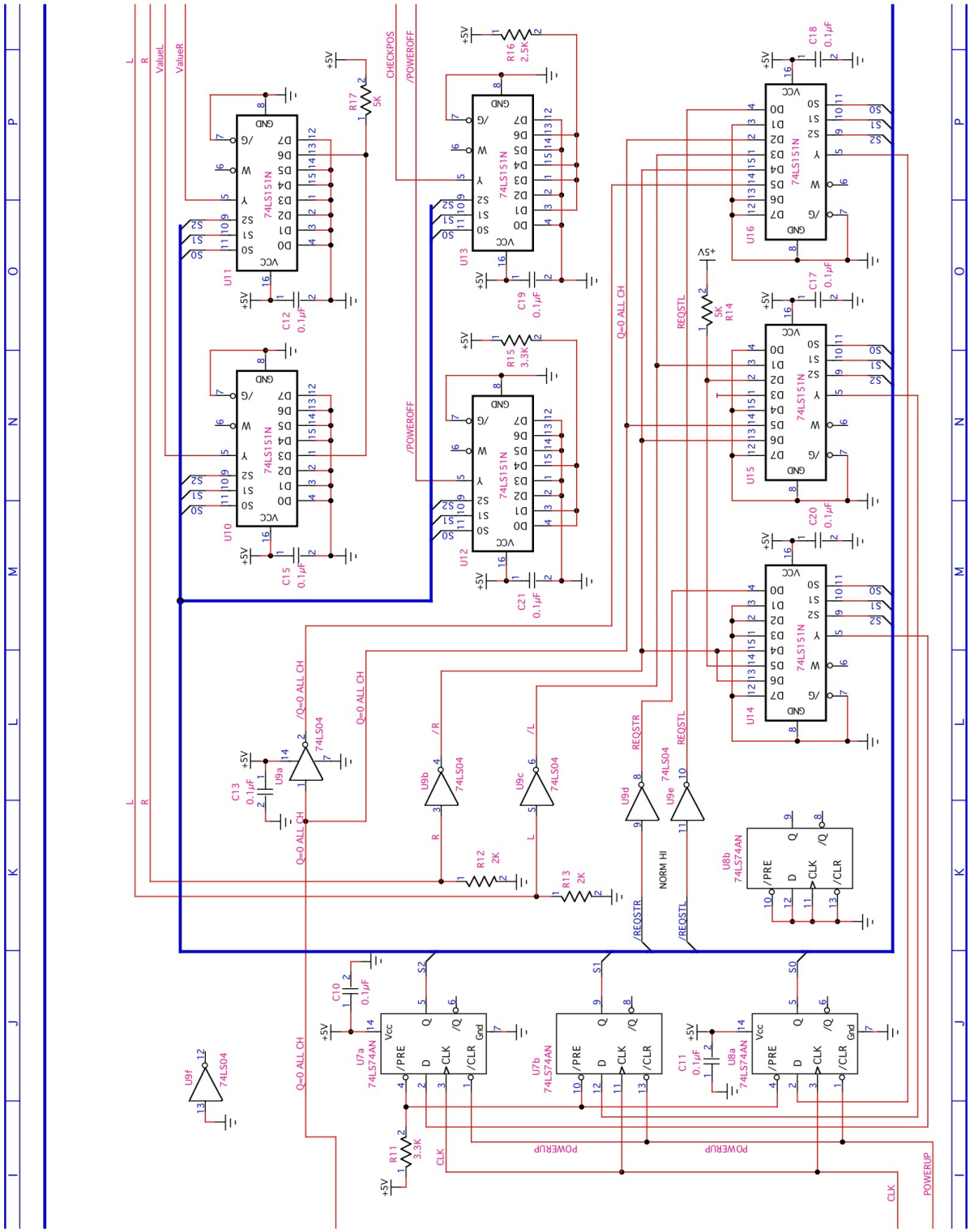

Figure B.8: Schematic of high voltage switching electronics for all channels (part 2 of 3)

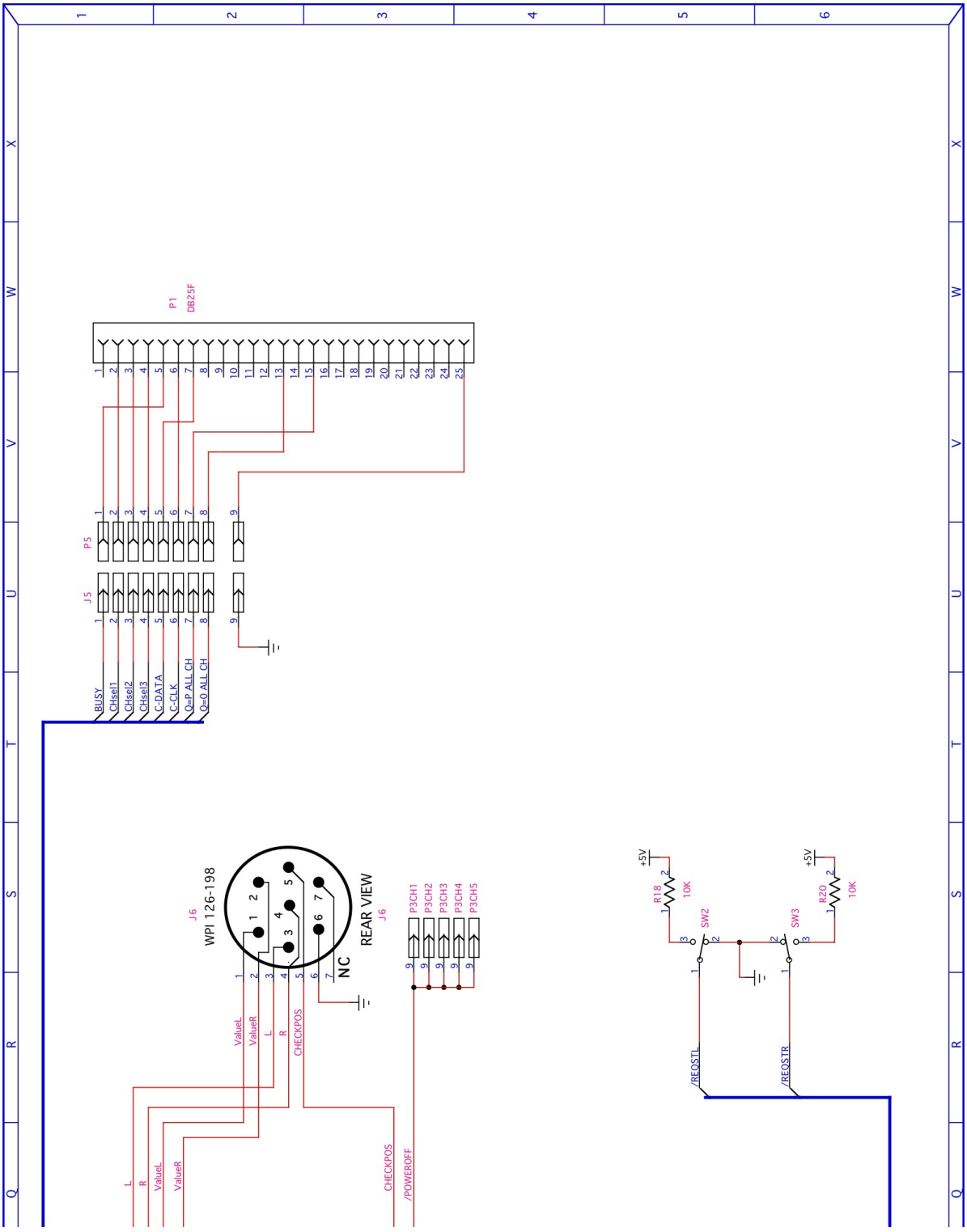

Figure B.9: Schematic of high voltage switching electronics for all channels (part 3 of 3)

Table B.2: User inputs and outputs of a single channel in the front panel

INPUT	FUNCTION
ON	Switch ON the channel
OFF	Switch OFF the channel
INT/EXT	The channel is operated by internally or by remotely
TRCK/ZERO	Track a given voltage or decrease voltage to zero
BCD	Voltage dialing input
TST+	+Reference voltage for the digital to analogue converter (D/A)
TST-	-Reference voltage for the digital to analogue converter (D/A)
OUTPUT	**DESCRIPTION**
PWR LED	Indicates that the high voltage is ON
TRCK LED	Indicates that the channel is tracking a given voltage
ZERO LED	Indicates that the output voltage is zero
LCD	HV display unit
V+	Programed output voltage (0 to TST+)
V-	Programed output voltage (0 to TST-)
HV SWCH	This will turn on corresponding high voltage power supplies in high voltage production and switching unit.

Table B.3: Control inputs and outputs of high voltage control unit state diagram for each channel

CONTROL INPUTS	
Name	**Description**
PWR UP	HIGH indicates power up logic
HV ON	Front button request for power on the channel
HV OFF	Front button request for power off the channel
HV IND	Relay engaged. Indicates that high voltage is ON
Q=0	Front button request for bringing high voltage to zero
CONTROL OUTPUTS	
Name	**Description**
$\overline{CLR}$	LOW clears the counters
HV Relay	Activate high voltage relay coil
$\overline{Powerdown}$	LOW sets counters to count to zero

Table B.4: Control inputs and outputs of the high voltage switching state diagram for all channels

CONTROL INPUTS	
Name	**Description**
PWR UP	HIGH indicates power up logic
$\overline{ReqstLeft}$	HIGH indicates the front button request for switch the LEFT
$\overline{ReqstRight}$	HIGH indicates the front button request for switch the RIGHT
L	HIGH indicates that the pneumatic valve has been pushed to the LEFT in the high voltage production and switching unit
R	HIGH indicates that the pneumatic valve has been pushed to the RIGHT in the high voltage production and switching unit
all zero	HIGH indicates that all voltages are Zero
CONTROL OUTPUTS	
Name	**Description**
CheckPos	HIGH check the position of the valve either LEFT or RIGHT, Feedback is taken through L or R inputs above
ValveLeft	HIGH push the valve to the LEFT
ValueRight	HIGH push the valve to the RIGHT
$\overline{Poweroff}$	LOW sets counters to count to zero, all the high voltages become zero

Appendix C

High voltage production and switching unit

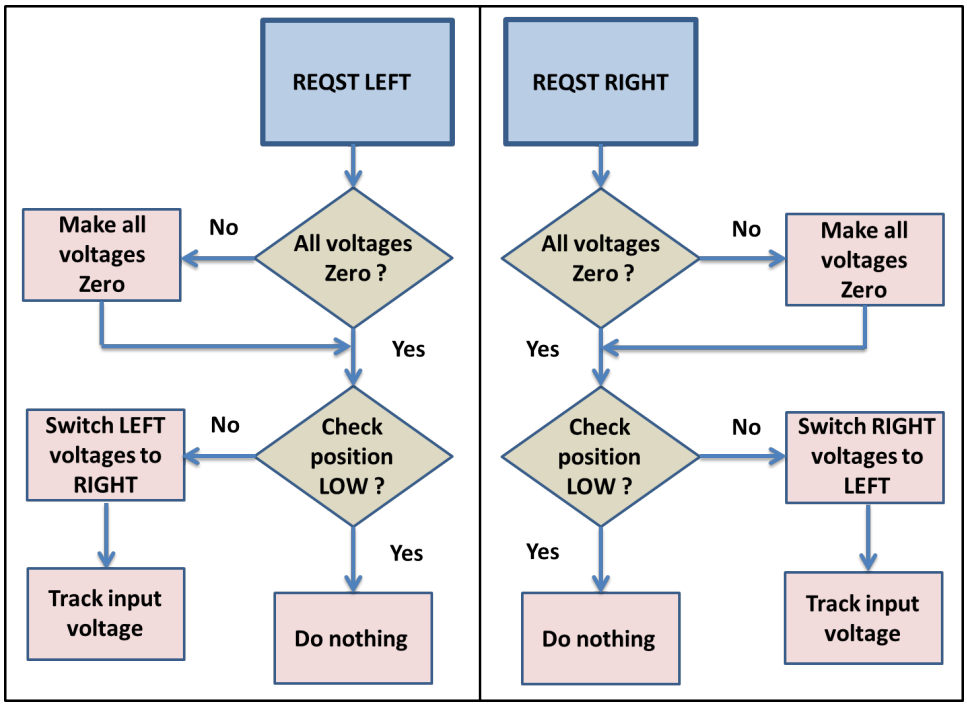

Figure C.1: Flowchart representation of high voltage switching mechanism

This unit contains high voltage power supplies(DC/DC comparators) and pneumatic controls for switching. The pneumatic valve is completely controlled by the control inputs CheckPos, ValveLeft and ValveRight. In addition to that it provides the feedback signals L and R to the high voltage control and switching electronics unit. Programed output voltages of each channel in the control unit are connected to the high voltage power supplies and they produce high voltages proportional to the inputs.

Fig.C.2 shows the schematic diagram of the function of this unit. Here, V1-V4 represent the bias high voltages for microchannel plates (MCP) in our time of flight

detector. When the pneumatic valve moves LEFT to RIGHT or RIGHT to LEFT all the output voltages are switched. This is happened only when all the voltages are zero.

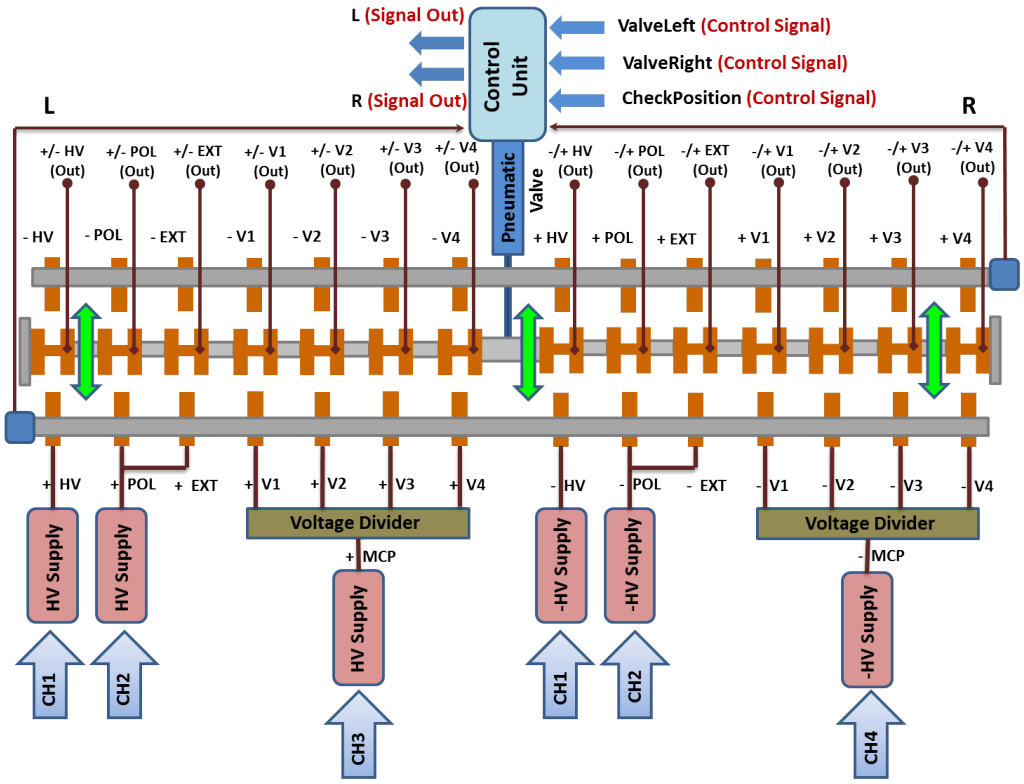

Figure C.2: Schematic of the high voltage production and switching unit

Appendix D

Remote control

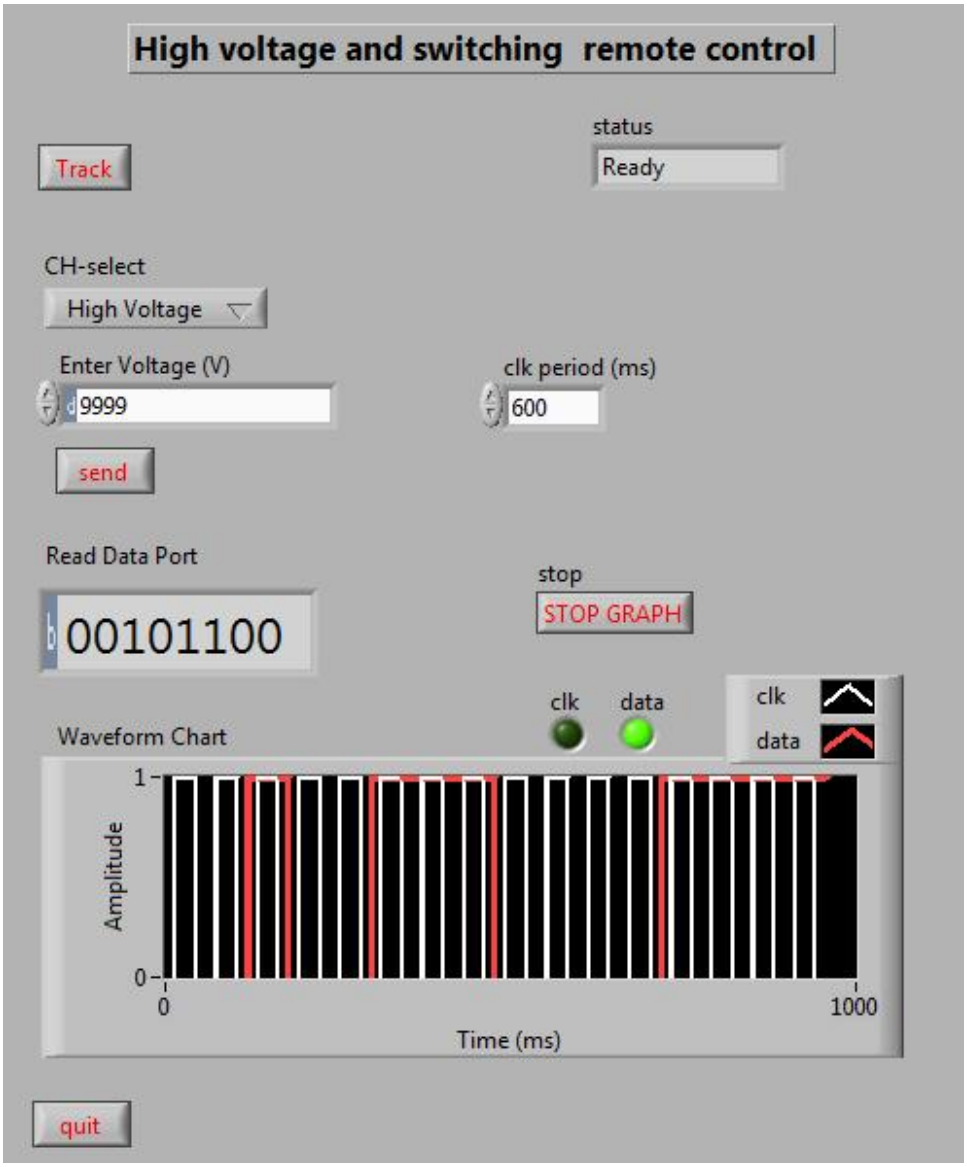

Figure D.1: Front panel of the remote control program.

This is the alternative way of inserting the magnitude of high voltage need to be produced instead of using BCD inputs in the front panel. We find this is convenient and

faster specially when we need to clean up the field plate by increasing and decreasing the voltage several times, until it reaches the final desired voltage. The front panel of the remote control program is shown in Fig.D.1. This interface communicates the device trough parallel port (printer port). First, the channel need to be selected and then the magnitude of the voltage need to be entered. Pushing "Send" button will send a binary array which corresponds to the input voltage to the electronics in that channel. Once, the "Track" button is pushed the channel will track that voltage. By changing "Clock period" the speed of the data sending process can be changed. All the control signals used in remote control program are shown in Table D.1.

Table D.1: Control signals used in remote control program

Name	**Description**
Busy	HIGH set the channel ready to accept data from the computer
CHsel	(CHsel1,CHsel2,CHsel3) is a three bit binary number that selects the channel which the data can be sent
C-data	A binary sequence which corresponds to the input voltage
C-clk	Clock signal produced by the computer in order to load the data
Q=P	HIGH indicates that all the channels are tracking their input voltages
Q=0	HIGH indicates that all the voltages are zero
G	Reference voltage ground for the data sent by the computer

Currently, the remote control program is setup to control the magnitudes of high voltages produced by the system. However, it can be easily modify to remotely switch high voltages as well. Necessary changes of electronics (master board) can also be done easily.